VILNIUS UNIVERSITY
FACULTY OF CHEMISTRY AND GEOSCIENCES
INSTITUTE OF CHEMISTRY
DEPARTMENT OF APPLIED CHEMISTRY

Justinas Januškevičius
Chemistry of Nanomaterials
Master thesis

SYNTHESIS AND CHARACTERIZATION OF YTTRIUM AND TERBIUM IRON PEROVSKITES AND YTTRIUM IRON GARNET

Supervisor assist. dr. Živilė Stankevičiūtė
Secondary supervisor prof. dr. Aivaras Kareiva

Date of submission _____
Registration No. _____

Vilnius 2020

TABLE OF CONTENTS

Abbreviations.

SEM – Scanning electron microscopy
XRD – X-ray diffraction
TGA – Thermogravimetric analysis
AFM – Atomic force microscopy
YIG – Yttrium iron garnet ($Y_3Fe_5O_{12}$)
TIG – Terbium iron garnet ($Tb_3Fe_5O_{12}$)
YIP – Yttrium iron perovskite ($YFeO_3$)
TIP – Terbium iron perovskite ($TbFeO_3$)
monoSi – monocrystalline silicon
polySi – polycrystalline silicon
RAM – Random access memory

INTRODUCTION

The perovskite structure has been receiving a lot of attention lately, driving discoveries and advancement in many fields – solar cells [1,2], gas sensors [3,4], superconductors [5–7] and many others [8–15]. Garnet is another very prominent structure that finds many applications in advanced technologies, starting with photonics [16], ending with biomedicine [17]. As such, simple synthesis procedures to obtain pure compounds of both these phases are quite useful. Furthermore, for many applications, synthesis of powders is insufficient; fabrication in a different form is required – such as coatings/layers [13,15,18] or nanoparticles [12,14,17], which is often complicated and expensive. For this reason, synthesis methods and procedures that could make this simpler and less expensive are always desirable.

Another topic that has experienced a recent surge in interest is that of magnetic materials. This has been driven by several factors, such as increasing interest in maglev technologies [19], the need for new technology in certain fields where current technology is approaching its limit (such as non-volatile memory) [20], and advancements in theoretical understanding of certain underlying principles behind magnetism and related phenomena (such as the now-famous article "Why are there so few magnetic ferroelectrics?"[21], which also led to a renewed interest in multiferroics). In fact, the entire field of spintronics is ever-developing, showing great promise to improve or replace many technologies that are currently in use [22]. Among the prerequisites for advancement of spintronics, some of the most important (besides engineering challenges and both more and deeper theoretical insights) are the development of new materials and their fabrication into layers, coating and nanostructures.

Combining the two previous topics, it seems logical to look for new magnetic materials among some of the most promising classes of ceramic structures – perovskites and garnets. The garnet structure, due to several interesting properties it displays, has already found use in some areas of spintronics, and perovskites are also showing potential. At the same time, to adhere to the requirement of the synthesis staying simple while still retaining capabilities of fabrication into different structures, the sol-gel method is also an obvious candidate due to its flexibility and simplicity. Due to all these reasons, this work attempts to combine all the previously mentioned elements, and employs the simple aqueous sol-gel synthesis method, dip coating, spin coating and membrane scaffolding to obtain a promising garnet phase (yttrium iron garnet is already established in the field of magnetics, though simpler and cheaper synthesis and fabrication is desirable), a related perovskite phase (yttrium iron perovskite has not yet found a widespread use, but has shown promise as a potential multiferroic, being synthesised and investigated before, though in limited capacity [23,24]) and another, different perovskite phase ($TbFeO_3$ has been synthesised before, but both synthesis and investigation has been carried out in a very limited capacity), and to compare these three related compounds.

The goal of this work:

To use the sol-gel method in order to synthesize pure yttrium iron garnet ($Y_3Fe_5O_{12}$), yttrium iron perovskite ($YFeO_3$) and terbium iron perovskite ($TbFeO_3$) powders, then attempt to fabricate coatings and nanomaterials of these phases, and also to investigate the properties of obtained materials.

Tasks:

1. To synthesize pure yttrium iron garnet ($Y_3Fe_5O_{12}$), yttrium iron perovskite ($YFeO_3$) and terbium iron perovskite ($TbFeO_3$) powders using an aqueous sol-gel method.
2. Utilise analogous sol-gel process as a basis for subsequent dip coating and spin coating in order to fabricate coatings on monocrystalline silicon.
3. Utilise analogous sol-gel process as a basis for fabrication of nanomaterials.
4. To carry out characterisation of obtained synthesis products.

1. REVIEW OF LITERATURE

1.1. Crystal structures

1.1.1. Perovskite

The perovskite crystal structure is a commonly occurring structure in natural minerals. It is named after the original perovskite mineral – $CaTiO_3$ – which was the first mineral identified to exhibit this structure [25]. More often, the word "perovskite" is used to refer to the entire group of ABX_3 structures (where A and B are cations, X is the anion), rather than this one particular calcium mineral. In part, this is probably because in more recent times, the entire structure class has received a lot of interest due to certain properties it exhibits [26,27]. The basic structure can be considered as a cube, with B cations at the corners, with one X anion in each face of the cube creating an octahedron, and the large A cation at the centre. It is one of the more substitution-tolerant structures available, allowing for a variety of substitutions while remaining stable [25], which can often be difficult to achieve otherwise (in fact, the number of possible compounds is so great, there are entire theories dedicated just to perovskite stability [28]). The cations can have 2+ and 1+ charges if X is a halide, and either 2+ and 4+ or 3+ and 3+ charges if X is oxygen. More exotic structures are also possible – for example halide perovskites where A or B (or both) are replaced by organic groups (this is popular in photovoltaics, especially, creating organic-inorganic hybrid solar cells [29], though it is used in some other fields as well). Double perovskites should also be mentioned here – these structures are achieved by replacing the single A cation with two different cations, each taking up half of the A sites. This is possible because perovskites are very versatile in terms of their crystal structure. This can be seen just by looking at the Goldschmidt tolerance factor, which is designed to give a rough estimate of stability and help engineer specific modified or distorted perovskite crystal structures by varying composition (though even for perovskites, if the variation is too great, certain structures would be too unstable, and so do not form – the tolerance factor partially correlates to stability) [10,28,30]. Many simpler perovskite structures are also relatively easy to manufacture, owing to their innate stability. All these and other factors have led to a variety of perovskites becoming a driving force in new materials for a wide range of applications, such as solar cells [1], gas sensors [3,4], catalysis [9], LEDs [11,12], superconductors [5–7] and others [13–15,31].

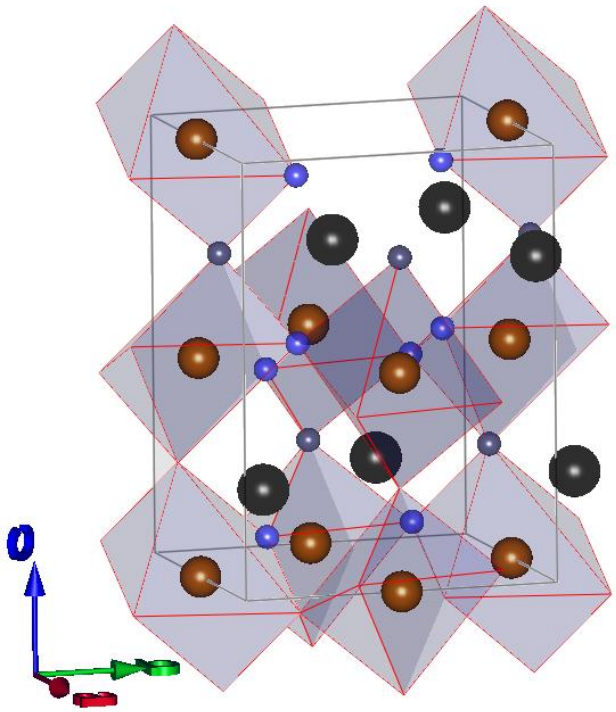

Figure 1. Terbium iron perovskite structure visualized (distorted perovskite structure). Data obtained from this work, with the aid of FullProf software and Rietveld analysis. Different shades of blue are oxygen atoms in different positions, black are terbium atoms, brown are iron atoms. In an ideal lattice, iron atoms would create a cube, the faces of which each would have an oxygen atom, which would form an octahedron, at the center of which would be the Tb atom.

In an ideal perovskite structure, the lattice is cubic, with B ion (the smaller ion) having 6-fold coordination can be imagined making up a cube, with X (mostly oxygen or halides – in the framework of this work oxygen is assumed, since that is most relevant to this work) occupying the edges of the cube, and the larger A cation showing a 12-fold coordination with oxygen, sitting in the middle [27]. This structure, while it finds some use, is not the one that attracts the most interest; as an example, if the structure is centrosymmetric, it cannot be ferroelectric [21]. Perhaps the more interesting structure, especially in the context of this work, is the "distorted perovskite structure. As the name implies, depending on the size of the ions, the perovskite structure can become distorted (example in Fig 1), so that the centrosymmetric quality is lost, and the structure is no longer cubic. This allows for some very interesting phenomenon (such as the aforementioned ferroelectric effect or piezoelectric effect) to manifest.

Considering this, control of the perovskite structure is important. Fortunately, there are theories which allow, to some extent, to predict the crystal structure depending on the composition. A relatively simple, widespread, though perhaps not always accurate (especially when it comes to structure stability [10]) theoretical factor that nonetheless allows for an initial evaluation, is what is called the "Goldschmidt tolerance factor". The factor is calculated by the following equation (considering ABX_3 perovskite structure):

$$t = \frac{r_A + r_X}{\sqrt{2}(r_B + r_X)} \qquad (1)$$

Where t is the Goldschmidt tolerance factor, and r_A, r_B and r_X are, respectively, the ionic radii of A, B and X ions [28]. If the factor equals 1 (or very close), then it indicates that if a perovskite structure is possible, it will likely be an ideal cubic perovskite structure, even though it does not guarantee that the structure will be stable – it only takes into account geometric, not chemical, superstructure, or other forms of stability [32]. The nature of the ratio is just that – geometric, since one of the properties of a cube is that the edge (which is $r_B + r_X$ for the perovskite structure) multiplied by $\sqrt{2}$ is equal to the diagonal of the cube (which is $r_A + r_X$ for the perovskite structure) [33,34]. It should come as no surprise, then, that ratios above or below 1 indicate that choosing ions that would in theory result in such a tolerance factor will create a distorted perovskite structure – as the tolerance factor moves further away from 1, distortions become higher, cubic structure is exchanged for structures of slightly lower symmetry, and stability decreases, making it less likely that the perovskite phase will be stable at all. Of course, atoms are not hard spheres like the theory assumes, and the exact tolerance factor that corresponds to a cubic structure can shift to some degree depending on the specific compounds – generally, the shift is to the lower side, with cubic structures reported even in the t=0.8-0.9 range [28,32]. The main distortions are of two types. The first is when the tolerance factor is t<1, which indicates the tilting of the octahedron in some direction (there exists a separate classification for the various potential ways that the octahedrons can tilt, which can have different consequences on the properties of the perovskite [35]). The other is when t>1 – this indicates that the B site is relatively small compared to the A site, and while the perovskite structure is less tolerant of this type of situation, it usually indicates a hexagonal structure [29,36]. For compounds chosen to synthesise in this work – namely yttrium iron perovskite and terbium iron perovskite, the approximate tolerance factors are 0.8 and 0.78 respectively, so a distorted perovskite structure is to be expected, which is what is aimed for in this case. This also fits relatively well with the tolerance factor theory. This "tunability" and theoretical tools to do so are both important and useful.

This is because perovskites can have a large variety of different useful properties, and tuning the structure can help to promote or enable those properties. As an example, the cubic perovskite structure is centrosymmetric, so the charges are evenly divided in the unit cell, and applying, then removing an external electric field does not leave any polarization – the material is paraelectric. However, if the centrosymmetric structure is disrupted (often the structure can change from cubic to, for example, tetragonal at lower temperatures, though some materials can have a ferroelectric structure at room temperature), applying, then removing an external electric field can cause a partial charge separation in the unit cell, and thus leave the unit cell polarized – this is known as the ferroelectric effect. In short, it means that the cell can experience a spontaneous electric polarization that is reversible by an applied external electric field [37,38]. This ferroelectric effect is useful for many applications (capacitors, ferroelectric RAM, sensors) [20,37]. And the ferroelectric effect is just one example. Taking theoretical considerations for the desired properties, a variety of effects can be enabled (or at least theory-motivated synthesis can be performed) by attempting to modify the crystal structure and composition accordingly – magnetic properties [39,40], piezoelectricity [41], desired band gap width [42], superconductivity [43,44] and possibly others.

1.1.2. Garnet

The garnet structure is also among the most prominent crystal structures in ceramic science. Initially, a group of silicate minerals were called “Garnets”. These natural garnets served as semiprecious stones and abrasives. Only around 1950s has progress been made which allowed to synthesise both these silicate garnets, and also (finally) synthetic non-silicate “garnet structure” ceramics [45].

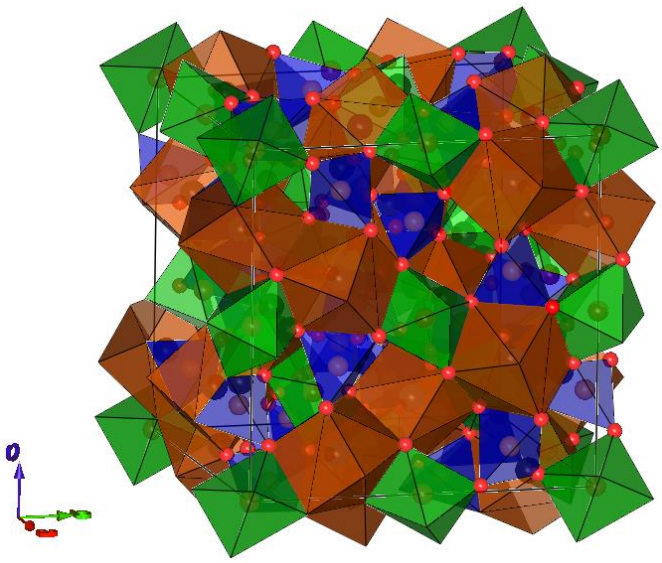

Figure 2. Yttrium iron garnet structure visualized. Data obtained from this work, with the aid of FullProf software and Rietveld analysis. The polygons represent atoms with different coordinations. Blue is Fe in tetragonal sites, green in octahedral sites, brown is yttrium in dodecahedral sites. Red spheres at the corners are oxygen atoms.

The general formula for garnet is $C_3A_2D_3O_{12}$, where O is oxygen and C, A and D are cations. The three cation sites are as follows – tetrahedral (D-sites), octahedral (A-sites) and dodecahedral (C-sites) with oxygen making up the corners of the structure [46]. However, this, of course, does not mean that all sites have to be occupied by different cations. Indeed, interesting effects can be achieved using the same cation in two sites – as an example YIG – yttrium iron garnet, which has the formula $Y_3Fe_5O_{12}$. Here, Fe^{3+} ions are in two different sites, with different spin orientations. Furthermore, the number of sites in a single unit cell is unequal – C and D sites outnumber A sites. What this results in are uncompensated spins, which, in turn, results in ferrimagnetic behaviour [47]. What cations will occupy which sites is primarily determined based on the ionic radii (and oxidation state) of the constituent cations. Obviously, most of the time, larger cations (with lower oxidation state) will

occupy larger sites (so the dodecahedral site will prefer larger cations, the tetrahedral site will prefer smaller cations) [46,48]. One thing to note is that the structure of garnet is relatively rigid, and space occupation within the lattice is relatively low. What this means is that while the garnet structure can accept a rather wide range of substitutions, the structure does not normally get distorted significantly and remains cubic [45]. If the ionic radius difference of the constituent ions is too high, it is more likely that no garnet structure will form, than that a distorted garnet structure would form [48]. The cubic structure can, under certain circumstances, be disrupted, but it requires certain specific situations – such as growing epitaxial films with large amounts of dopants [45].

In terms of properties, the already-mentioned stoichiometric and geometric considerations of the crystal can give rise to magnetic properties – such as the mentioned ferrimagnetism. Other than that, garnets, especially aluminium garnets such as YAG (yttrium aluminium garnet) are good crystal hosts that can be used for solid state lasers [49]. Also, another reason garnets have been drawing the interest of researchers recently is because they can exhibit magneto-optical effects, such as Faraday rotation, among others. What this allows to do is to create tuneable optical modulators, for example – modulators that rotate the plane of linear polarization depending on the applied magnetic field [16], magnetic field sensors, and finds other specific uses in various fields such as photonics [50–52]. Overall, garnets exhibit some interesting and unique properties that are found in few other materials, and so development in the field of garnet ceramics is always important to advance the fields in which they are used.

1.2. Sol-gel synthesis and structurization

The sol-gel synthesis method has grown into one of the most popular methods for ceramic synthesis, along other staples of the field such as solid-state, hydrothermal, microwave and co-precipitation syntheses [53]. The precursors for the method are generally metal salts, which, at the start, are dissolved in the solvent. If a proper solution is formed, the method is sometimes called a “solution sol-gel” synthesis, to differentiate from a sol-gel process that uses a stable dispersion of particles (a true sol – that is a system composed of a solid phase dispersed in a liquid phase). For the aqueous method, traditionally, alkoxide salts were used, though for a modified process (originally known as the Pechini process), simple nitrate, chloride, sulphate or similar salts can be used. If the solvent is organic, carrying out the synthesis becomes a bit more complicated from a technical perspective and more expensive compounds that can be dissolved in the organic solvent become necessary (metal alkoxides or other similar compounds with organic ligands are generally used). In modern days, organic solvents are, most of the time, used when the aqueous method does not work well – for example if the compounds are sensitive to water, if the product does not form under aqueous conditions or other similar reasons, since the aqueous method is generally less toxic, cheaper and metal salts are more available (since not all metals have stable alkoxides).

In case of the traditional aqueous route, water hydrolyses the -OR groups of the dissolved alkoxides, and partial condensation between the compounds begins. For the non-aqueous route, water is usually added separately to start hydrolysis – this means there is more control over the hydrolysis step, since it is not tied to the solvent. It should be noted that the rate of hydrolysis depends on the pH of the solution. Acidic and basic conditions act to catalyse the reaction, while neutral conditions result in a slower reaction. As for the modified sol-gel process using inorganic metal salts, obviously, no reaction occurs upon dissolution, so a complexing agent (ethylene glycol, citric acid or a combination are among the

most popular) is added which complexes the metal cations. The purpose of this is twofold – the organic ligands act as fuel for the eventual calcination process if ceramics are the goal (and this process is usually used exactly when ceramics are the goal), and also – more importantly perhaps – they allow for an interconnected network to be formed by reactions between the ligands, similar to the traditional sol-gel method. An important point here is also the pH, which has an even bigger impact than for the traditional sol-gel method. It needs to be carefully considered because not only does it work as a catalyst, but also affects cation binding to ligands and works to prevent hydroxide precipitate formation (especially important in mixed-metal systems), so a balance needs to be reached. At this point, all three described processes (that is, traditional alkoxide sol-gel, non-aqueous sol-gel and modified sol-gel) converge – after hydrolysis (or complexation for the modified process) reaches an appreciable degree, condensation reactions begin to some degree, forming polymer-like structures, fine particles, and potentially anything in between – this is still considered a sol. The proper polycondensation step is usually carried out at near room-temperature (often slightly higher). When a proper, interconnected network is formed (rather than just separate particles), it is usually considered that the sol becomes what is known as a "wet-gel". It is called such to separate it from sol – which does not yet have an interconnected particle network, only separate partially connected fragments (or is simply a solution, in the early stages), and to separate it from dry gel (or xerogel) – when most of the solvent is evaporated from the wet-gel [54–58]. Sometimes, the gel is left for an additional "ageing" step, since the reactions occur continuously, so allowing time for them to settle more can sometimes improve results, though, at the same time, the system may not always be stable, and leaving the sol to sit for too long, can cause precipitate to form or other undesirable outcomes.

Finally, depending on the structure that one is attempting to manufacture, different processing options of are available (during various stages of the process). One type of processing – supercritical drying of the wet gel, which produces an aerogel [59]. This is based on avoiding the capillary forces associated with crossing the liquid-gas phase boundary, which normally crushes the relatively fragile structure of the gel, and instead using elevated temperature and pressure in order to convert liquid into gas avoiding the phase boundary – that is by turning the liquid phase into a supercritical fluid first, then gas. Meanwhile, evaporation of water from the wet gel crossing the liquid-solid phase boundary produces a dry gel/xerogel, which can have its own uses [60], or which can be sintered at high temperature to produce ceramic powder particles.

Coatings can also be obtained in a few ways – with spin coating and dip coating being the two most popular processes [61–63]. To elaborate, dip coating is a procedure where the substrate is submerged into the sol vertically, then slowly withdraw, causing the capillary forces to retain some of the sol, while the rest undergoes gravitational draining. As the substrate is lifted out of the sol, many processes start at the same time – the outer liquid layer flows back into the sol, while the inner layer "sticks" to the surface due to capillary forces. A streamline appears dividing the upwards and downwards moving layers of liquid. At the separation point where the outer layer peels off, the inner layer is exposed to air and the solvent begins to evaporate (pore formation often occurs at this point due to competing forces). After that, as the inner layer dries and the thin layer of liquid sol rapidly turns into gel (generally a matter of seconds), a drying line becomes visible, followed by colourful parallel lines caused by interference. The drying line is nicely parabolic if the substrate withdrawal rate equals drying line velocity. When the deposition is complete, the substrate can then be calcinated to create a ceramic coating. Dip coating is a

relatively simple process to carry out from a technical perspective, which makes it quite attractive, and it is also quite simply upscalable, even if it does require large baths of the sol. However, it's a process that is somewhat complicated from a theoretical perspective. Many competing forces act on the film deposition region (viscous drag, gravitational force, surface tension are the main ones, though other smaller forces can have influence as well) and determine the streamline position. Some fluid-dynamics formulas are available, though of limited practical use [61,64]. Because of this, real-world application involves some trial-and-error to adjust the substrate withdrawal rate, sol concentration, viscosity and withdrawal mode in an experimental way to be optimal, so the theory is more useful in terms of knowing the general principles governing the process rather than being able to carry out calculations for desired results. This allows to optimise film thickness and other parameters depending on the desired application. While dip coating is often considered a method to produce uniform m coatings, defects – such as thickness gradient towards the bottom – can arise, but can also be fixed by optimization of the process.

Spin coating, while relatively similar, does nonetheless have some important differences. For spin coating, film formation involves spreading of the sol on the substrate that is horizontally placed on some kind of rotatable fixture (usually, the substrate is held in place by vacuum suction), followed by centrifugal draining (the rotation causes the sol to spread along the surface, while any excess flung away by the centrifugal force), and lastly the evaporation of the sol. In some ways, using centrifugal force can allow for greater control of the film through the choice of angular velocity, whereas for dip coating, the withdrawal velocity range is much more limited (though also adjustable). As a result, spin coating has a somewhat smaller reliance on sol viscosity, and can sometimes make it easier to control layer thickness (though as the layer gets thinner, the resistance to flow increases, and more and more force is needed to reduce the thickness of the film, limiting how thin the films can be made). While both centrifugal draining and evaporation are happening simultaneously, spin coating is separated into two stages, where at the first stage the process is predominantly determined by viscous flow, and at the second stage by evaporation. The fact that both processes happen at the same time can sometimes result in radial ridges – that is ripple patterns moving outwards from the centre. This is caused by tiny local surface force imbalances, which act as a starting point that causes ripples. As the layer dries, the liquid becomes too viscous for ripples to appear. This only occurs in some systems. Alkoxide sol-gel route is one example where it may occur, due to alcohols released into the solution during hydrolysis. Since they have a faster evaporation rate than water, it causes the surface layer to be water enriched, possibly accelerating hydrolysis/condensation and increasing average surface tension. However, if this occurs, it can usually be avoided by preventing evaporation during spinning, as an example. It should also be kept in mind that if the liquid is non-Newtonian (that is, viscosity stress arising from flow is not linearly correlated to strain rate at all points) the coating thickness may not be uniform (thicker around the middle if the liquid is shear thinning – that is if its viscosity decreases under shear strain) [65]. Besides the already mentioned processing techniques, a variety of other specialised options are available (such as the membrane-assisted nanotube synthesis used in this work).

For this work, sol-gel synthesis was chosen because of several reasons. The most important perhaps is that since structurization can influence the properties and applicability of garnets and perovskites to a very large extent (dimensionality can affect superconductivity, magnetoresistance and Curie temperature for example [66,67]), considering it is important. As already mentioned, sol-gel synthesis allows for a wide variety of options in terms of structure fabrication and has potential for upscaling (since it is

generally similar to “one-pot” synthesis that can often be encountered in organic chemistry) [57]. It is fair to mention, at this point, that for some uses of garnets, epitaxial growth of monocrystalline coatings is the most desirable type of result, since some properties only appear for monocrystalline coatings, or are most pronounced that way, and the sol-gel process is not widely known to produce monocrystalline coatings, outside some potential outliers [68]. However, to be fair, most other common methods of ceramic synthesis are not capable of this either – specialised methods are required. Despite this, in most other areas of application, the sol-gel method, as already described, offers many options for fabrication into a wide variety of other useful structures, like few other methods of synthesis.

1.3. Magnetism

Magnetism is a phenomenon that involves the emergence of magnetic fields and their interactions. At the most basic – it is a consequence of the fact that all elementary particles have an intrinsic property of spin (defined by the spin quantum number), giving atom nuclei a net spin, and also giving each electron a spin. A particle that has a charge and a spin then creates a magnetic momentum (has a magnetic field). These particles also have mass, which means they also have an angular momentum. The total angular momentum must always be conserved, and since it consists of the angular momentum and the magnetic momentum, changing one affects the other. More complex interactions are possible when materials, rather than atoms, are considered, and even more so where crystalline compounds are concerned. Full, proper explanation of the nature of magnetism, such as there is, starting with the origin of spin, involves a combination of quantum mechanics and special relativity theory, and has both separate chapters in books about condensed matter or solid state physics [66,67], and also entire books [69] dedicated to it, that can be referred to in order to expand on the short description already given. As such, it is more productive, in the scope of this work, to look at theories relating to specific magnetic phenomena and how to enable them from the standpoint of material engineering, though some topics of quantum mechanics that would provide context are unavoidable.

Identical particles and exchange interaction. One of the most important phenomena to understand when talking about the emergence of magnetism in crystals is the exchange interaction. It is a quantum mechanical effect that occurs between two “Identical particles” as described by quantum physics (that is, particles that are not distinguishable between each other – electrons can be considered among such particles). For the purpose of understanding exchange interaction, identical particles must first be explained. What is important about identical particles, in simple terms, is that in order for them to be identical, exchanging them has to result in no observable changes, for example no changes on the probability density of the particle. And the probability density is, by definition, the square of the wavefunction:

$$|\psi(r_1, r_2)|^2 = |\psi(r_2, r_1)|^2 \qquad (2)$$

Where r_1 and r_2 are the two particles, ψ is the corresponding wavefunction. So, for there to be no change in the probability density when exchanging two electrons (or other particles), the wavefunction too, has to remain unchanged (such wavefunctions are called symmetric for the exchange of two particles), or change only in sign (wavefunctions called antisymmetric):

$$\psi(r_1, r_2) = \pm\psi(r_2, r_1) \qquad (3)$$

Particles for which the sign does not change are called bosons (photons are among such, as are all other particles with integer spin), and for which the sign changes are called fermions (electrons are among them, as are other particles with half-integer spins) [70]. If we were to map out the probability density of symmetric and antisymmetric wavefunctions by r_1 and r_2 (positions of each electron), their form would not change, as per identical particle requirement, but what we would notice, is that for the symmetric function, the maximum probability density would appear in two places where $r_1=r_2$, while for the antisymmetric function everywhere where $r_1=r_2$ would equal 0. This leads to the conclusions that particles that have a symmetric wavefunction bunch together (since $r_1=r_2$ shows maximum probability density), while particles that have an antisymmetric wavefunction repel each other. This is a general quantum mechanical phenomenon, and is observed even for particles without charge, though it interacts with charged particles in an additional, special way [71]. This antisymmetric property of fermions, it might be mentioned, also leads to Pauli exclusion principle, because if two fermions would occupy the same state, the new state ψ_n would be a linear combination of the two possible states, one of which has a negative sign by definition of fermion, as shown earlier:

$$\psi_n(r_1, r_2) = c[\psi(r_1)\psi(r_2) - \psi(r_2)\psi(r_1)] = 0 \qquad (4)$$

Where c is some constant. The product is 0 at all points, so it is apparent that the probability density would be 0 at all points, which, in short, means that it would not exist – in other words, this means that two electrons cannot occupy the same space [70]. This is important for exchange interaction as well later. It should also be noted here that electrons (which are the focus for magnetism) have two wavefunctions that describe them – the spatial (orbital) wavefunction and the spin wavefunction. If we were to label spin up as "a" and spin down as "b", and the two interacting electrons as 1 and 2, we would have 4 different possible states – α(1)*α(2), α(1)*β(2), α(2)*β(1) and β(1)*β(2). States 1 and 4 are symmetric, while states 2 and 3 are neither symmetric nor antisymmetric, so we have to construct two spin functions that have symmetry properties, just like in eq. 4.:

Symmetric: $$\frac{1}{\sqrt{2}}[\alpha(1)\beta(2) + \alpha(2)\beta(1)] \qquad (5)$$

Antisymmetric: $$\frac{1}{\sqrt{2}}[\alpha(1)\beta(2) - \alpha(2)\beta(1)] \qquad (6)$$

Where $1/\sqrt{2}$ simply assures that the total wavefunction normalizes to unity. This means there are four combined spin states – three symmetric (those are α(1)*α(2), β(1)*β(2) and eq. 5) and one antisymmetric (that is eq. 6). Therefore, two electrons can have two different combined spin states – a symmetric state (called the triplet state), where the combined spin quantum number S=1 (since the three symmetric states are as follows – both spin up, which is +1, one spin up one down, so 0, and both spin down, which is -1, so spin quantum number emerges by analogy to the orbital quantum number where quantum number 1 means the same combination of -1, 0 and 1), and a single antisymmetric state (singlet state), where the spin quantum number is S=0 (one spin up one down). This is leads us to exchange energy. It is very important to note that the requirement for electron wavefunction to be antisymmetric only applies to the overall wavefunction (this is why we did not ignore the symmetric spin wavefunctions), which is made up of the spin (χ) and the spatial (ψ) wavefunctions. If both are symmetric ($\psi_s\chi_s$) or antisymmetric, ($\psi_a\chi_a$) the result is a symmetric wavefunction, which breaks the overall antisymmetric requirement, and such states do not occur and are not observed. The other two possibilities fulfil the overall antisymmetric

requirement; one is the singlet state if the spatial wavefunction is symmetric and the spin wavefunction is antisymmetric ($\psi_s\chi_a$). This is how two electrons occupy the same orbital in their ground state – symmetric space function means the two-electron state has the maximum probability density if the positions of the electrons match, while the antisymmetric spin function means the spins are opposite. The other possibility (most important to us, since exchange energy emerges here) is the triplet state, which is when the spatial wavefunction is antisymmetric, and the spin function is one of the three symmetric spin states ($\psi_a\chi_s$). Exchange energy is what arises if one tries to calculate the energy of these new states, integrating their probability density and taking into account Coulomb interaction (energy is derived by multiplying electron Coulomb interaction energy by probability that electrons will have some separation r). What this results in is an integral of fours terms – two that are equal and account for the mentioned Coulomb interaction (E_1). The other two terms (negative for singlet state, positive for triplet state) are also equal, but they account for energy (E_2) that arises from the difference between symmetric and antisymmetric states – that is, since for symmetric spatial state the electrons are much closer together, there is a large energy increase from Coulomb interaction (also, since electrons repel each other, and are closer on average too in this case, they screen each other's interaction with the nucleus more as well), while if the electrons are in an antisymmetric state, they are further apart on average, which means a weaker Coulomb repulsion (and also less screening of the positive atomic nucleus, which allows both electrons to interact stronger with it, decreasing overall energy). Basically, E_2 is a correction to Coulomb interaction that arises from symmetric and antisymmetric states. [67,71].

Emergent magnetism. This directly relates to magnetism, since a purely classical explanation cannot really account for magnetic properties. Because what it means is that if two unpaired electrons from different atoms are close enough together, exchange interaction occurs, which makes it better for both of them to have an antisymmetric spatial wavefunction, since it (by increasing expected distance between electrons) allows to reduce Coulomb repulsion (and nucleus screening) and have a lower overall energy. This means that their spin wavefunctions are symmetric (to adhere to the antisymmetric requirement of the combination of spatial and spin wavefunctions), and the spins align (this ferromagnetism mechanism is known as "direct exchange"). Of course, exchange interaction decreases exponentially with distance, so spins will only align if two main conditions are met. First, the exchange energy has to be significant enough to overcome the magnetic dipole repulsion from orienting the two spins in the same direction. If the exchange interaction is weak enough, then magnetic dipoles will arrange themselves antiparallel to minimise energy from magnetic repulsion, and antiferromagnetic ordering will be the result. This, however, is a very weak effect, and any more meaningful influence is only observed at very low temperatures. For real solids, this is not the main reason for antiferromagnetic ordering; the more important reason is that for some systems, ferromagnetic ordering means neighbouring electrons cannot "hop" through different sites, since it would break Pauli exclusion principle, while antiferromagnetic ordering allows it, even if it is not energetically favourable, but this causes the wavefunction to be delocalised, decreasing energy (more about this later). Second, aligning all spins in one direction also minimises entropy, so the exchange energy has to be enough to overcome entropic considerations. This is also where Curie temperature comes from – simplifying, it is the temperature where the exchange interaction E becomes lower than kT term (where k is Boltzmann constant and T is temperature in Kelvins). When a temperature is reached where the influence of entropy becomes higher than exchange energy, ferromagnetic ordering is lost and the spins arrange themselves

in a paramagnetic fashion. Diamagnetism was also not mentioned yet – in short, diamagnetism is an intrinsic property present to some extent in all materials to resist an external magnetic field, that is, for most materials, almost entirely based on the number of electrons. However, it is a rather weak effect, so if other forms of magnetism are present, its influence is usually neglectable by comparison, outside some specific scenarios (certain weak types of paramagnetism can be overcome by diamagnetism, also, superconductors have specific properties which make them very strong diamagnetics). Also, in solids, various other scenarios can arise – for example, if a crystal lattice has more than one variety of atom, the ordering can be antiferromagnetic, but the two different varieties can have magnetic moments of different magnitudes, resulting in net magnetic moment (even if it is weaker than ferromagnetic) – this is called ferrimagnetism [67,69,72].

Indirect exchange. Coming back to ferromagnetism, direct exchange is rarely the main cause of ferromagnetism – in solids, the distance between two cations is too great, and neighbouring magnetic orbitals do not have significant overlap. Exchange interaction is still the main cause; however, the difference is that it often works more indirectly – for example through an intermediary atom.

One such mechanism, perhaps most common for non-conducting solids, is superexchange. It is an indirect exchange interaction between non-neighbouring magnetic ions, mediated by a non-magnetic ion between them. At the most basic, it results in antiferromagnetic ordering, since it reduces energy by allowing the wavefunction to be delocalised. If we were to take a cubic cell as an example – let us say the atom configuration is M-O-M, where M is metal and O is oxygen. If we were to consider that M has one free electron in the outer shell, antiferromagnetic configuration of spins would align as follows: ↑; ↑↓; ↓ (where the spin configuration of each atom is separated by a semicolon, arrows indicate electrons with indicated spin, and empty spots will be indicated with an underscore). This allows, in theory, for an electron to jump in various ways, for example: ↑; ↑↓; ↓→↑; ↓; ↑↓→_; ↑↓; ↑↓. While such jumps may not occur to any meaningful degree in practise, the possibility itself allows electron delocalisation and lowers the overall energy of the system. This would not be possible for ferromagnetic ordering, since the spin cannot change during a jump, and Pauli exclusion principle disallows two electrons of the same spin to be in the same place. This effect often easily overcomes the weak influence that would favour ferromagnetic ordering from direct exchange. This is a common mechanism for antiferromagnetic ordering in perovskites. Superexchange can also, in some specific circumstances, result in ferromagnetic ordering [69].

Another important related mechanism for magnetism in solids is double exchange. If we were to consider the same arrangement of metals and oxygen M-O-M, for double exchange to occur the two metal ions would have to be in different oxidation states. Then, ferromagnetic exchange can be favoured, since it would allow (this time real) electron hopping: ↑; ↑↓; _→↑; ↓; ↑→_; ↑↓; ↑. Not only that, if the spins are aligned, then upon entering its new orbital, the electron would already be aligned with any other unpaired electrons in that orbital, decreasing the Coulomb repulsion with them, as per the exchange interaction within the orbital. And even if not, the interaction is strong enough that it is still favoured, even if all the electrons in that orbital have to rearrange to match the exchange interaction. This highlights just how strong the effect can be sometimes [69].

There are other numerous possible interactions, depending on the particular system. For this reason, to summarize the general tendencies, the Goodenough-Kanamori rule was formulated to account for various interactions. It states, for example, that for superexchange, two half-filled orbitals interacting at

180° will produce antiferromagnetic ordering, while if one of the orbitals are filled or empty, ferromagnetic ordering will be the result. Also, that if two half-filled nearest orbitals are instead at a 90° angle, while weaker, exchange interaction can still lead to ferromagnetic ordering [73].

While these explanations are rather heavy from a theoretical perspective and dive more into the fields of quantum mechanics and condensed matter physics rather than just inorganic chemistry and crystallography, understanding how magnetic properties emerge provides a very helpful tool when attempting to carry out synthesis of materials that would exhibit the desired properties.

1.4. Multiferroics

Multiferroic materials are not something entirely new to science. They are materials that combine both ferroelectricity (electric polarization hysteresis) and magnetic properties (ferromagnetism, ferrimagnetism, antiferromagnetic or similar), preferably in a single phase. However, the topic had lost some interest for a time, since no sufficiently good multiferroics could be found ($BiFeO_3$ displayed multiferroic behaviour in single phase at room temperature, but had other problems – weak ferromagnetism, large dielectric loss and leakage current, difficult synthesis due to volatility of bismuth [74]). Lately, however, the topic has experienced a resurgence. There are several reasons for this – better theoretical understanding of the underlying principles of multiferroicity and targeted synthesis of magnetic materials, need for new technological solutions (since improvement on some current technologies is reaching its limits), and the advancement in science that enables new or improved synthesis and investigation of properties.

Potentially, multiferroics have the capacity to be the driving force that could improve several key technologies. Proper multiferroics should have the property which allows their magnetisation to be controlled using an electric field (which would be much more energy efficient) and their electric polarisation to be controlled by magnetic fields. This could improve a large number of already existing technologies. Also, multiple state memory elements could potentially be created, having up to 4 states per unit instead of the regular 2, which would be a very large improvement for memory storage [21,74–77]. Because of how important these effects would be for technology, numerous attempts have been made to create room-temperature multiferroics, though success to create a multiferroic that would have the desired properties still eludes researchers.

2. EXPERIMENTAL

2.1. Materials and equipment

Materials: yttrium nitrate ($Y(NO_3)_3 \cdot 6H_2O$, Alfa Aesar, 99.9%); terbium oxide (Tb_4O_7, Alfa Aesar, 99.9%); iron nitrate (Duro-Galvanit-Chemie, 98%); polyvinyl alcohol ($(C_4H_6O_2 * C_2H_4O)_n$, partially hydrolised, Mw approx. 70000, Merck Schuchardt OHG); ethylene glycol (Aldrich, 99.5%); nitric acid (Eurochemicals, 65% concentration); Si substrate (Orientation [100], p-type, doped with boron, CrysTech); Si substrate (polycrystalline, Elkem, Norway); polycarbonate membrane filters (*Membrane filters (Isopore track-etched polycarbonate)*, MiliPore™, pore diameter 0.2 μm, membrane diameter 25 mm).

Equipment: furnace SNOL E5CN-H; X-ray diffractometer Rigaku MiniFlex II (Japan) operating with Cu $K_{\alpha 1}$ radiation under Bragg-Brentano configuration; scanning electron microscope Hitachi SU 70; plasma cleaning and polymerisation equipment (Nano, Diener Electronic); simultaneous thermal analyser Perkin Elmer STA 6000 (gels were heated in an air flow (20 mL/min) at a heating rate of 10 °C/min); AFM (Veeco Bioscope 2 atomic force microscope); Mossbauer spectrometer (Wissenschaftliche Elektronik GmbH; ^{57}Co(Rh) source); magnetometer used consisted of a lock-in amplifier SR510 (Stanford Research Systems), a gauss/teslameter FH-54 (Magnet Physics) and a laboratory magnet supplied by the power source SM 330-AR-22 (Delta Elektronika) (magnetic and Mossbauer measurements carried out in Centre for Physical Sciences and Technology); dip-coater KSV Dip Coater D and spin-coater SCS P6700.

2.2. Synthesis procedure

Sol-gel synthesis. First, the terbium precursor had to be converted from an oxide into a nitrate salt. For this purpose, 0.8124 grams (1.0865 mmol) of terbium oxide (Tb_4O_7) were added to 8 mL of concentrated nitric acid. Nitric acid was then evaporated using a heated magnetic stirrer (avoiding reaching a boil). To ensure most residue of nitric acid was removed, a small amount of deionized water was added, then evaporated, repeating the cycle three times. The remaining solid – terbium nitrate – was used in subsequent synthesis of its sol. The initial solutions were made using the as-prepared terbium nitrate and yttrium nitrate ($Y(NO_3)_3 \cdot 6H_2O$). The nitrates were dissolved in 20 mL of deionized water (respectively, 3.1142 grams (8.1309 mmol) yttrium nitrate for yttrium iron garnet (YIG), 4.7653 grams (12.442 mmol) for yttrium iron perovskite ($YFeO_3$), as-synthesized terbium nitrate for terbium iron perovskite $TbFeO_3$). Then, stoichiometric amount of iron nitrate ($Fe(NO_3)_3 \cdot 9H_2O$) was dissolved in 50 mL (or 25 mL in case of terbium) of deionized water. The solutions were mixed and left to stir in covered beakers for one hour at 60°C. After that, ethylene glycol was added (in a 1:1 molar ratio to metal ions in the solution) as a complexing agent and left to stir for an additional two hours. Part of the solution (10 mL) was then separated for gelation and sintering to obtain powders, the rest was kept for coatings and nanostructurization. To obtain ceramic powders of the materials, the separated solution was left to stir at 60°C in an uncovered beaker until the gel formed. After the formation of the gel, temperature was raised to 120°C and the gel was left to dry for 24 hours. A small amount of gel was kept for thermogravimetric analysis (TGA). The remaining material was removed from the beaker, ground into fine powder and heated for 2 hours at 800°C, using a heating rate of 10°C/min. The obtained powders were then sintered again at 1000°C for 10 hours, using a heating rate of 1°C/min [78–80]. These final obtained ceramic powders were then investigated by x-ray diffraction (XRD) and Mossbauer spectroscopy.

Fabrication of coatings. Initially, coatings were prepared by a dip coating procedure, using silicon as a substrate. First, to prepare the silicon substrates, 2x1 cm sized p-type silicon (surface plane 100) substrates were placed in a freshly prepared 3:1 mixture of H_2SO_4 and H_2O_2 (commonly known as the "piranha solution") and left there for 15 minutes. The substrates were then removed, washed using running deionized water, and left in a dilute 2% solution of hydrofluoric acid (HF) for 5 minutes. Again, the substrates were then removed and washed under running deionized water. Surface was then activated using oxygen plasma. The previously mentioned solutions of metal salts and ethylene glycol were mixed with a 3% polyvinyl alcohol solution at a ratio of 1:1. Dip coating procedure was then carried out, using the prepared silicon substrates and the mentioned solution, with a submerging speed of 85 mm/min., retention time of 10 seconds, and a retrieval speed of 40 mm/min. After the dip coating procedure, the newly-formed coatings were left to dry for 30 minutes, then placed in a heating oven and heated at a rate of 1°C/min. up to 500°C, with a retention time of one hour. This coating-heating cycle was repeated 15 times, after which the final heating was up to 1000°C for 10 hours [78], so the ceramic would form. The procedure for 5-layer coatings was the same, except repeating the cycle 5 times instead of 15. The coatings were then investigated using SEM, XRD, AFM and Mossbauer spectroscopy; magnetic measurements were also carried out. Spin coating was also employed, using 1x1 cm sized p-type silicon substrates (surface plane 100). In this case, the substrates were simply washed with deionized water, then acetone. The solution used was the same as the one for dip coating. Spin coating parameters were as follows – 500 RPM reached in 2 seconds, retained for 5 seconds, then 1000 RPM reached in 2 seconds, retained for 5 seconds, then 1500 RPM reached in 2 seconds, retained for 90 seconds, then deceleration to 0 over 20 seconds. The second set of parameters used was the same, except the third acceleration was up to 2000 RPM instead of 1500 (still reached over 2 seconds – so faster acceleration). When the deposition of the film using the spin-coater was complete, the coatings were left to dry for 10 minutes. Then, the coatings were placed on a hotplate set to 120°C for 5 minutes, then placed into a furnace set to 400°C for 10 minutes. Finally, they were left to cool for 5 minutes. The spin coating and heating procedure was repeated for the same substrate 5 times, creating 5 layers, at which point the sample was placed in a furnace to heat to 1000°C, 1°C/min for 10 hours, in order to turn the coatings into ceramic.

Fabrication of nanotubes. The nanotubes were also prepared using the initial solutions of metal nitrates and ethylene glycol by the means of a sol-gel hard template assisted method [81]. In this case, polycarbonate membranes (pore width of 0.2 μm) were dipped in the solution for 1 minute, then excess liquid was removed using paper and the membrane was left to dry for 10 minutes, repeating the dipping-drying cycle 5 times. Two membranes were prepared for each material – one was placed on polycrystalline silicon, the other on monocrystalline (surface plane 100) silicon. The samples were then heated at a rate of 1°C/min. to a temperature of 550°C for 5 hours. The resulting nanotubes were investigated using XRD and SEM. Based on the results, this procedure was repeated using only monocrystalline silicon, changing the heating temperature to 800°C and retention time to 3 hours. An attempt was also made to synthesise more nanotubes by stacking up 3 membranes on each other, one after each heating cycle.

3. RESULTS AND DISCUSSION

3.1. Thermogravimetric analysis

Thermogravimetric analysis (Fig. 3) was used in order to determine any major physical or chemical events the gel undergoes during the heating process. This was needed in order to determine a reasonable temperature range in which experiments could be performed – and later adapted or modified.

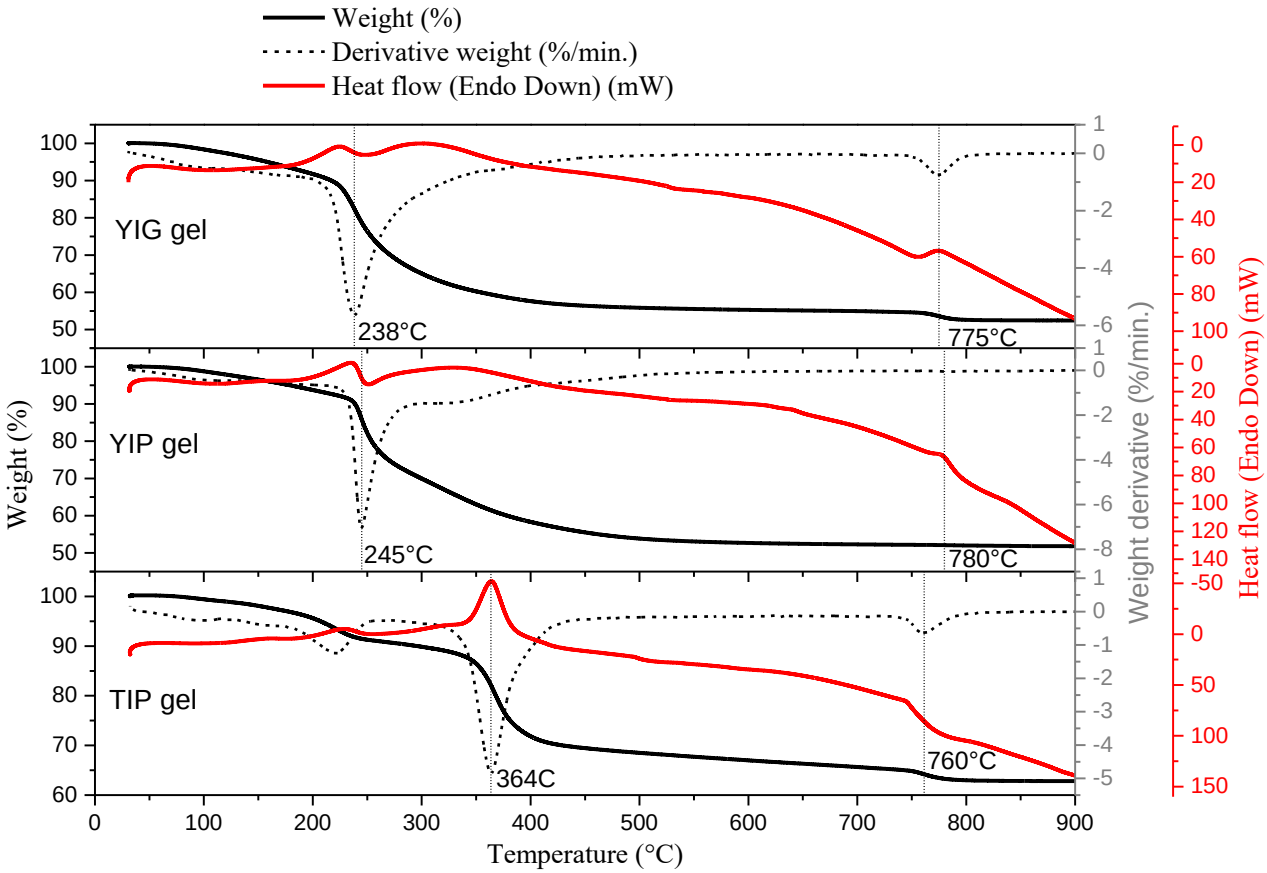

Figure 3. Thermogravimetric analysis of YIG, YIP and TIP gels.

Thermogravimetric analysis shows clear mass-loss peaks indicating the main processes taking place during the reaction. For yttrium compounds, a major loss of mass is seen that peaks at approximately 240°C. For terbium this peak is further – at around 360°C. These peaks most likely correspond to the major part of the organic material undergoing burning. Mass loss then stays low for all samples (the small, consistent loss with increasing temperature observed could be remainder organics and nitrates) up until it reaches a second small peak at about 760°C, which most likely indicates loss of any remaining volatiles and formation of final phase (as also indicated by the heat flow change, which is visible even for $YFeO_3$ sample, which doesn't show a loss of mass, but still shows a change in heat flow at the same temperature, most likely indicating phase formation).

3.2. X-ray diffraction analysis

3.2.1. Powders

Powders of yttrium iron garnet, yttrium iron perovskite and terbium iron perovskite were synthesized by a wet chemical sol-gel method. First, X-ray diffraction was carried out in order to determine if the chosen synthesis procedure was suitable to obtain pure phases of these compounds (Fig. 4).

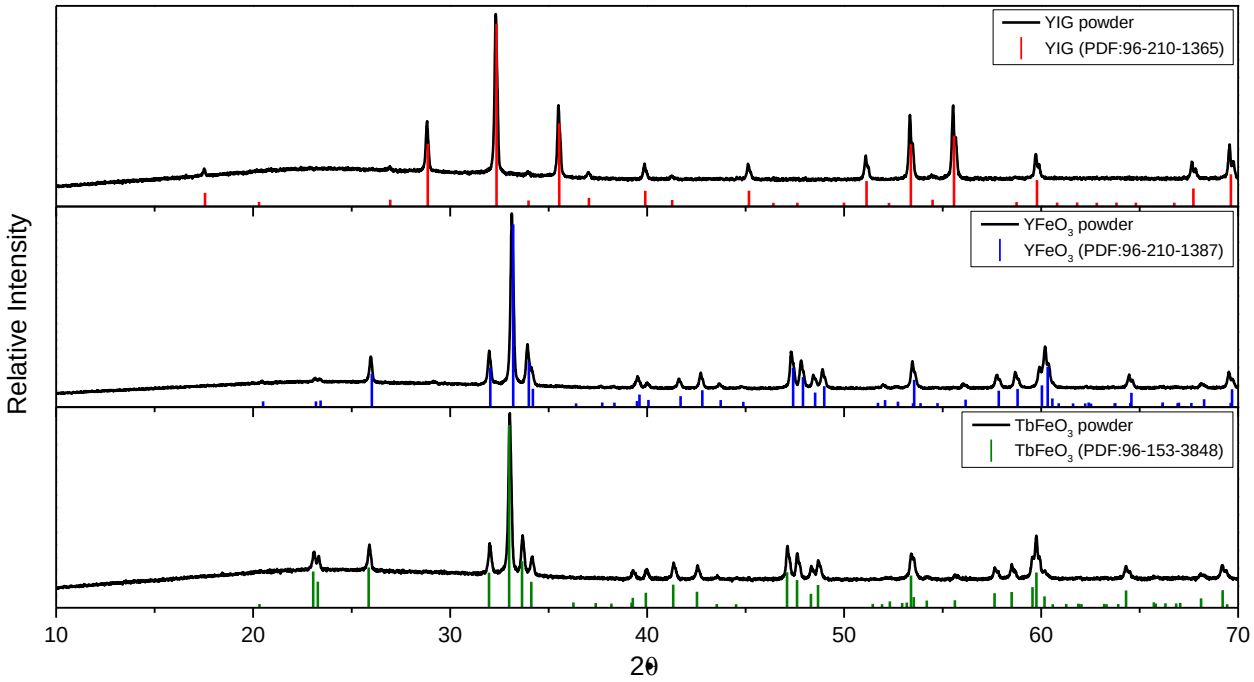

Figure 4. XRD patterns of pure powders of indicated ceramics obtained by sintering the gels at 1000°C.

As can be seen from the diffractograms, powders of all three materials are monophasic, and match reference patterns near-perfectly in both position and intensity, with no clear peaks of secondary phases visible. This indicates that the synthesis process chosen is suitable for the formation of pure powders of yttrium iron garnet, yttrium iron perovskite and terbium iron perovskite.

3.2.2. Coatings

Structure fabrication was one of the goals of this work. For this reason, the sol-gel process was employed in conjunction with dip coating and spin coating processes to create ceramic coatings on monocrystalline silicon. In addition to what was already mentioned in the “Review of Literature” section, dip coating is a method well-suited for preparing thin layers and coatings from chemical solutions. Benefits of the method include low cost, control over coating thickness, ability to be applied to flat panels, cylinders, or other objects with complex geometry or large surfaces. Meanwhile, spin coating is best suited to flat shapes, offering fast drying time and good uniformity, but low material efficiency, generally utilising only about 5% of the dispensed material, with the rest being flung off into the coating bowl and lost. Both methods offer their own advantages and are widely employed in both industrial and scientific settings. Just to reiterate – fabrication of coatings has enabled or improved countless technologies, and because of this, it is an important area of research to explore [65,82–86].

For the ceramic coatings fabricated in this work, X-ray diffraction analysis was performed for samples made using the *dip coating* procedure (Fig. 5), and later, when spin coating was carried out based on those results, for samples made using the *spin coating* procedure as well (Fig. 6). This was important in order to determine whether the results from powders (pure, single phases of desired compounds) carried over when making coatings using the same initial solution from the sol-gel process.

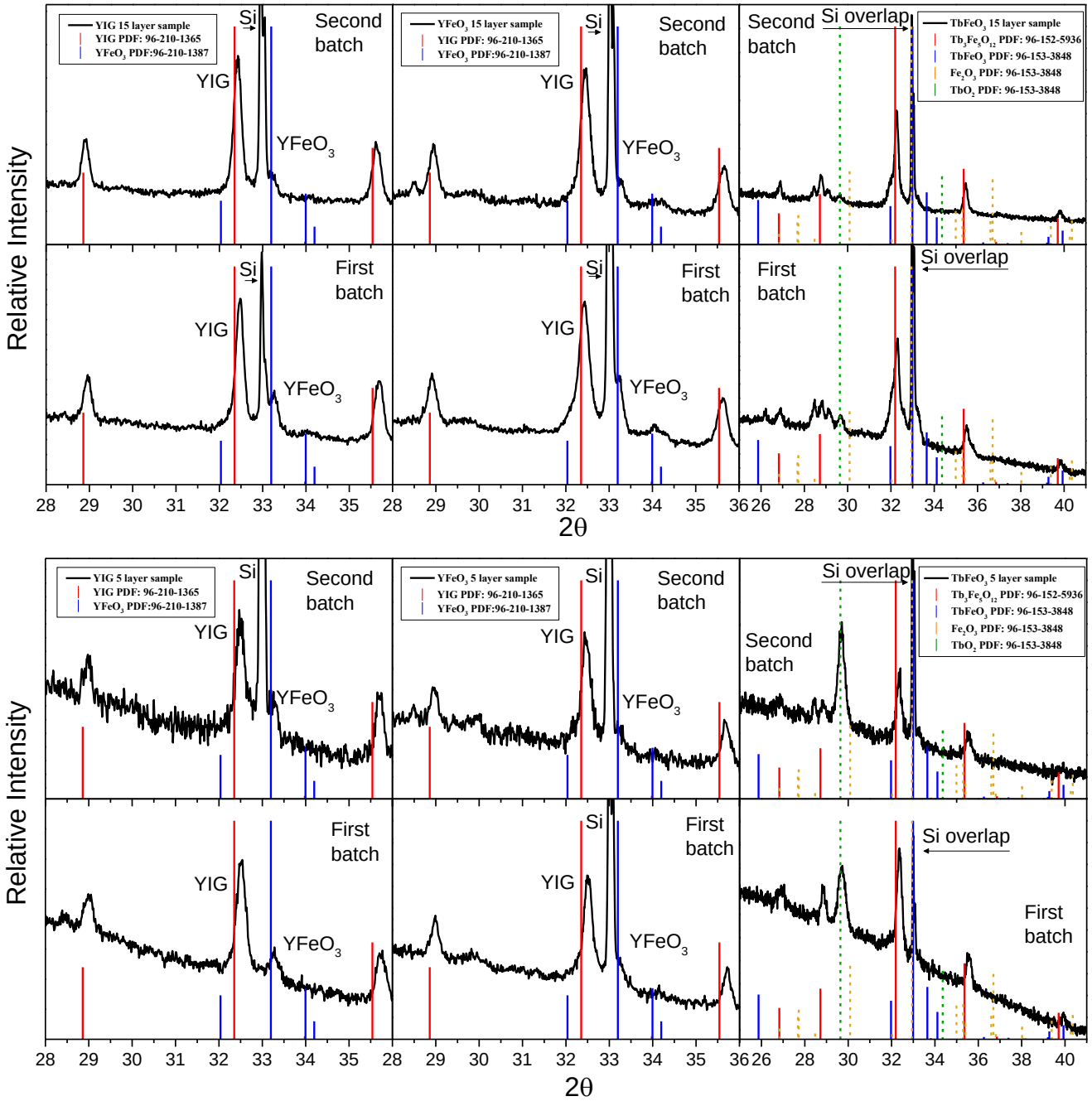

Figure 5. XRD patterns of 15-layer (first two rows) and 5-layer (bottom two rows) ceramic coatings (dip coated), samples indicated in the labels. The same label applies both to the first and second batch of samples. The diffractograms are zoomed in to the most relevant region for clarity.

The outcome of experiments, when using the same solution that was used for powders in order to make coatings, was very different. As can be seen from Fig. 5, several problems arose. The main problem was the fact that the silicon peak (the high-intensity, narrow peak at 33°, though absent in several samples) from the substrate partially overlaps with the main peak of YIP (at about 33.2°), and also overlaps with the main peak of Fe_2O_3 (at 33°). This means that YIP is sometimes observed as a partially merged peak with Si. While it can still be seen as a moderately separate peak for YIP (usually enough for identification), the problem is exacerbated for TIP, where the main perovskite peak position overlaps with Si near-perfectly. Normally, the phase could likely be identified by secondary peaks, but the high background due to low amounts of material, and potential partial orientation due to it being a coating (which could be skewing peak intensities), complicates this. One feature that helps with identification in this case is the fact that the silicon peak is very high intensity and very narrow, so the more diffuse peak around the base of the intense Si peak can still be observed to a degree. The same applies to the main peak of Fe_2O_3. Iron oxide was not observed for any of the yttrium-containing samples, but it could not be completely ruled out for terbium-containing samples, since the overlap is closer, and since TbO_2 peak was observed, which indicated that unreacted iron oxide could also be present. No unreacted yttrium oxide was observed for yttrium compounds, however.

One other feature to note is that in all yttrium (and possibly terbium) samples, regardless of whether the stoichiometry of the initial solution was that of $YFeO_3$ or $Y_3Fe_5O_{12}$, both garnet and perovskite phases formed with nearly the same peak intensity ratio. Most likely, this is because of the dip coating procedure chosen – an assumption can be made that when the silicon substrate is withdrawn from the solution, the adhesion stoichiometry gravitates to a certain ratio of Y/Fe, regardless of the stoichiometry of the solution.

The two different batches of coating samples showed good repeatability, as the coating process for the two different batches was carried out several months apart (sol was kept refrigerated for the duration), but still showed very similar XRD results. As can be seen from the diffractograms, the repeatability, while not perfect, is reasonably good – almost all the peaks are in the same positions and have the same, or similar, intensity, excluding the main perovskite peak, which showed more variation.

Due to the results of dip coating and suspected stoichiometry distortions caused by specific surface interactions during the dip coating procedure, it was decided to attempt to use the same solution, but switch the coating technique to spin coating. It was assumed that this, in theory, could reduce the influence of surface interaction on the results, especially if a larger acceleration and lower top speed is chosen. Faster acceleration should cause less-specific removal of excess solution, since surface interaction should have a smaller contribution to the total force acting on the liquid, while slower top rotation speed should leave a larger amount of liquid, thus less solution in direct contact with the surface, and thus lower surface interaction that way. The acceleration time was kept to 2 seconds in all cases, while top-speed was changed (which also means a higher acceleration speed for higher top-speed samples). The results can be seen in Fig. 6.

The diffractograms show a significant difference in relative peak intensities of the perovskite and garnet phases. Whereas for dip coating, the garnet phase/perovskite phase main peak ratio was about 4/1 for most samples, here, the ratio is closer to 2/3 for YIG, 4/3 for YIP and 1/1 for TIP samples. This is more promising, since a difference indicates some degree of control might be possible. Unfortunate side effect was that for TIP, a large single peak that was potentially TbO_2 was visible, though this cannot be confirmed definitely, since it is only a single peak, and its second most intense peak was not observed.

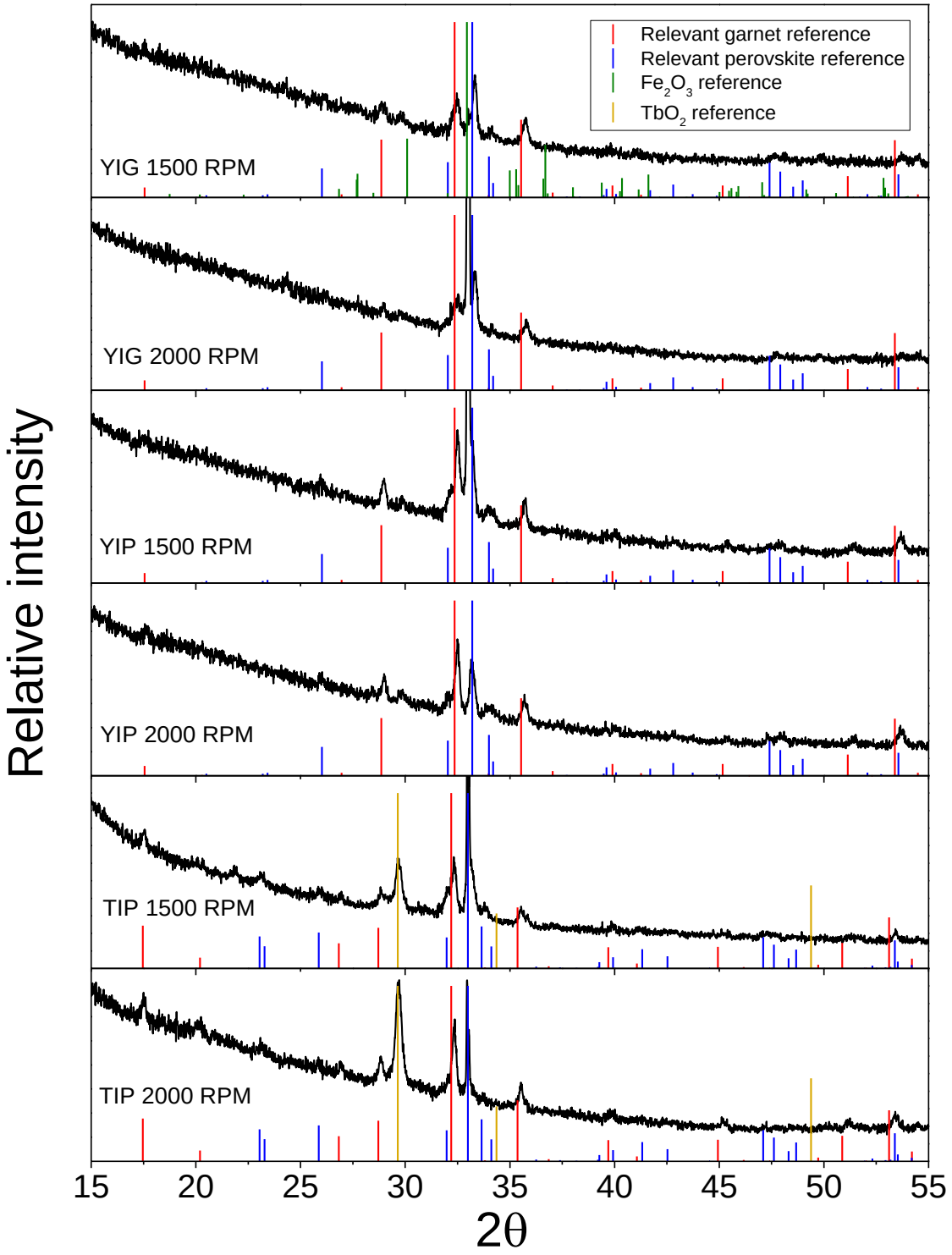

Figure 6. XRD patterns for indicated spin coated samples of YIG, YIP and TIP.

3.2.3. Nanotubes

While coatings have an established place in technology, nanomaterials by comparison are still in a state of growth, with some technologies having already adapted these new structures, and others still very much in the process of adaptation. One-dimensional nanostructures such as tubes, wires, rods and others

have attracted interest due to their applicability in electronics, optoelectronics, sensors and biotechnology. Possibly among the greatest challenges preventing such materials from becoming a staple in many technologies is that synthetic approaches for diverse morphologies of such materials remain limited [87,88].

As part of the goal of this work, an attempt was made to extend the applicability of the same sol-gel process by adapting it for nanomaterial synthesis. Fig. 7 displays the diffractograms of nanotubes heated at 550°C.

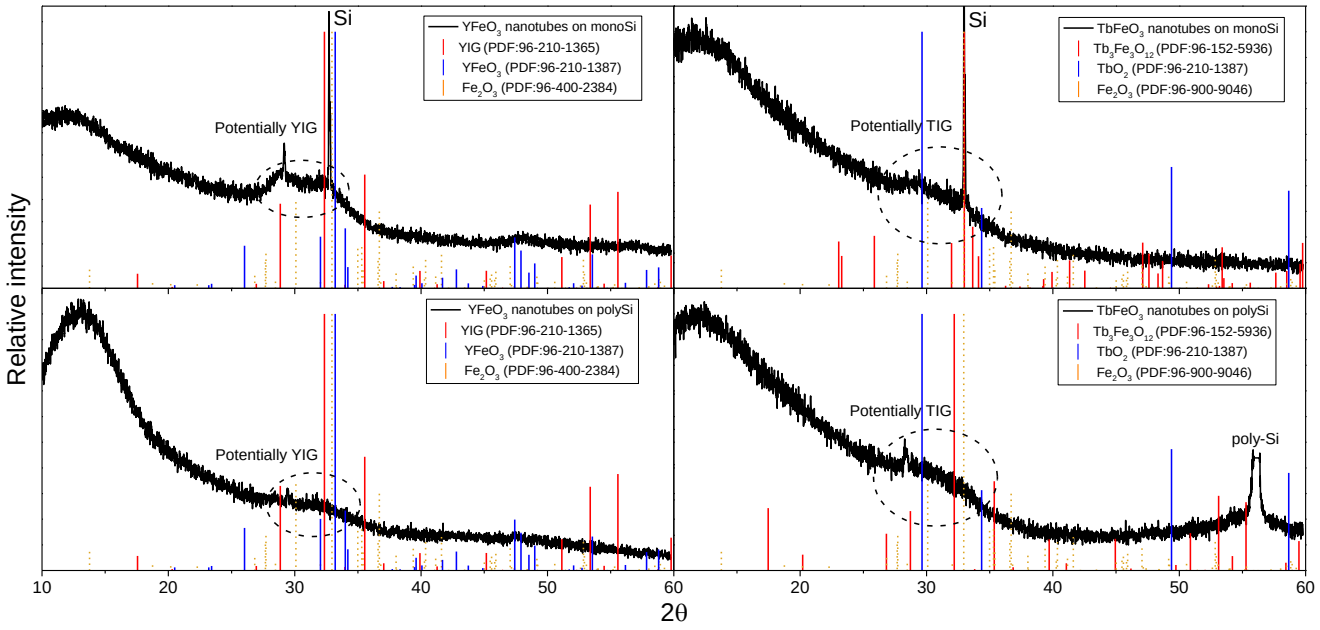

Figure 7. XRD patterns of perovskite nanotubes heated at 550°C on either monoSi or polySi (garnet phase not displayed, since no nanotubes formed).

The absence of any sharp, noticeable peaks is immediately apparent. In fact, there are only traces of what could potentially be the beginnings of peaks. This is not very surprising, considering the TGA results discussed earlier (the first major loss of mass should be over by 550°C, but for the second -and final- process to occur the sample needs to reach a temperature of 800°C). Even so, hints of some early-stage-ordering can be seen even at this stage (areas of interest are marked by traced line ellipses in Fig. 7). If there was no ordering whatsoever, this area would be a flat line, as opposed to a raised area being visible. Despite that, there is clearly no crystal phase formed yet. Even so, the results are interesting when considered in conjunction with SEM images for these samples (discussed in the SEM section) and they are also useful for comparison reasons as well (to see whether any crystal phase is visible after the first major event seen in thermogravimetric analysis). Lowest possible heating temperature is preferred, because otherwise there is a possibility of nanotubes being sintered together and losing their characteristic structure.

Considering the results of the first experiment, and that no clear crystal phase formed, the second batch of nanotubes was heated to a higher temperature of 800°C. This temperature was chosen based on TGA data, since the main phase formation should be finished by this point. Higher temperature increases the chances of the nanotubes fusing together, so it was decided to keep the temperature at 800°C and use a shorter heating time (3 hours instead of the 10 used for powders).

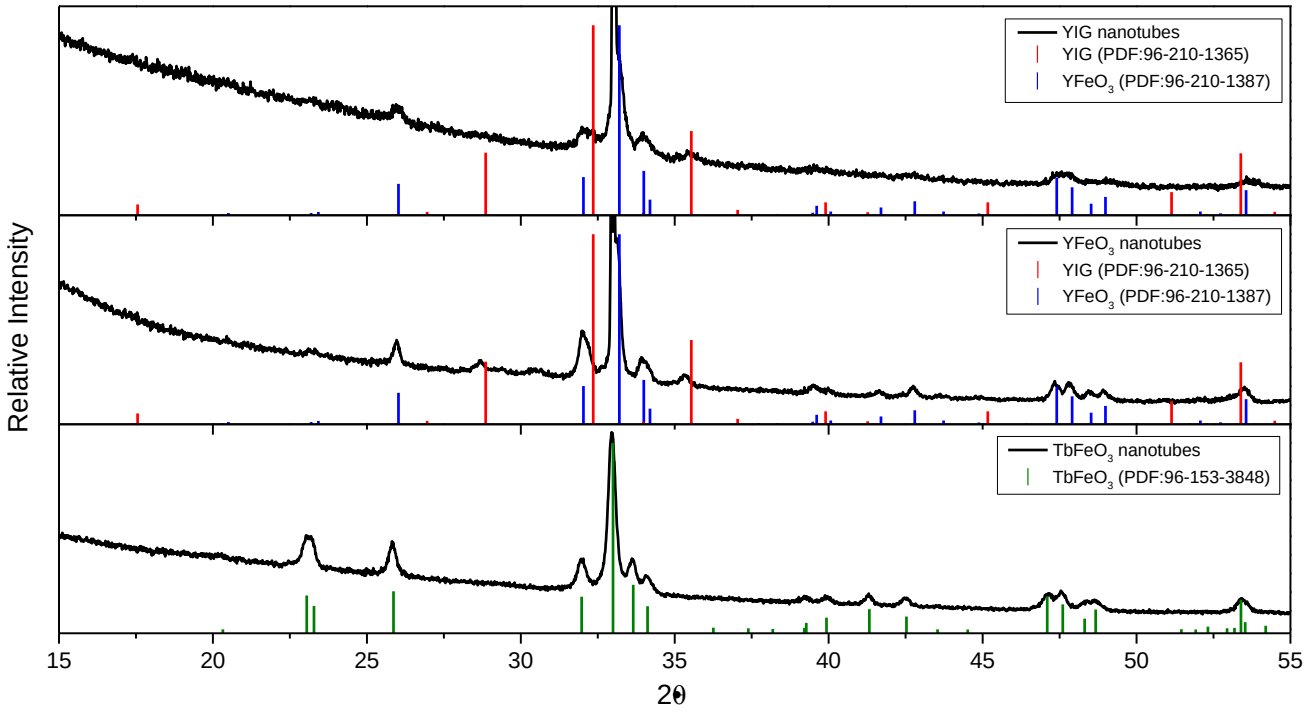

Figure 8. XRD patterns of perovskite and garnet nanotubes heated at 800°C on monoSi.

The results displayed in Fig. 8 show that, unlike for samples heated at 550°C, clear, well-defined crystal phases are visible. Several other features of this diffractogram are noteworthy as well, however. The first is that for yttrium compounds, in both cases, it seems like a mixture of garnet and perovskite phases formed. There is enough evidence supporting this when looking at secondary peaks that match rather well, even if the main perovskite peak is difficult to identify, due to the intensive Si peak that is partially merged with it for both yttrium samples, and even if the main garnet peak is low intensity, and potentially fused with a secondary perovskite peak, due to how diffuse both are (this was not a problem before, since for coatings, the garnet phase had much more intense peaks, so the secondary perovskite peak did not interfere with phase identification). For the garnet sample, lack of a well-expressed garnet phase is likely due to the lower temperature and retention time, since garnet usually requires a higher temperature [78,79]. What is surprising, however, is the diffractogram of terbium perovskite. It shows only the peaks for terbium iron perovskite, with no peaks that would indicate any secondary phase – no garnet, unreacted oxides, or anything else; the diffractogram is very similar to the terbium iron perovskite powder diffractogram – only the peaks are slightly wider, not as sharp. The fact that no garnet phase formed likely indicates that it requires somewhat more specific conditions, though if that is the case, terbium garnet formation for dip coating samples remains an interesting development, since it was not observed here or for powders.

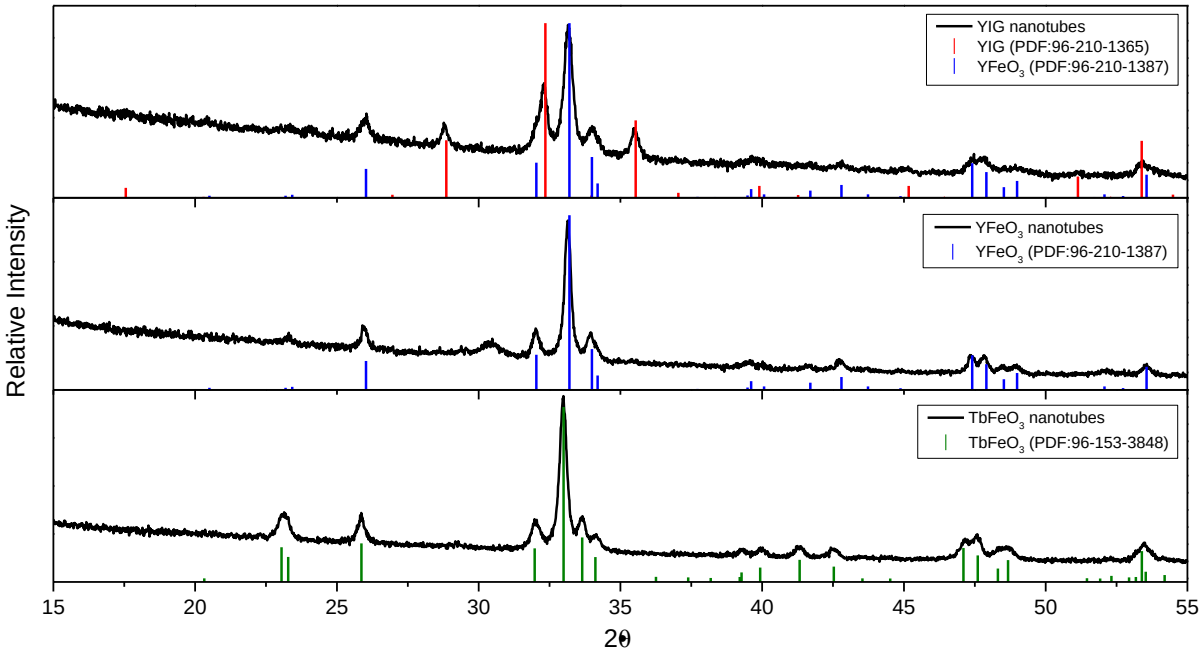

Figure 9. XRD patterns of perovskite and garnet nanotubes made by layering 3 membranes one by one – carrying out heating at 800°C after each layer.

An attempt was then made to upscale the process to some degree (to allow more accurate measurements and test upscaling possibilities) by stacking the membranes on the silicon substrate in layers. The results (Fig. 9) show that, at the very least, phase quality did not deteriorate. In fact, quality is increased in some ways. This is likely due to repeated heating, which allowed more time at high temperature for a clearer garnet phase to form rather than anything else. For both perovskite samples, no garnet phase is visible, though yttrium iron perovskite does show a single unidentified, low intensity peak at 31°. Due to it being a single and diffuse peak, it could not be definitely matched to any particular phase. Furthermore, the peak does not match the main suspect secondary phases – yttrium oxide, iron oxide or yttrium iron garnet either. One other positive feature when stacking more layers is that identification is made easier due to the characteristic, intensive Si peak being absent in this case, likely because the nanotube layer was thicker, and so Si signal was not caught.

3.3. Scanning electron microscopy

3.3.1. Coatings

SEM images of coatings were acquired in order to evaluate coating quality and to see if there were any important surface features or differences between the samples, since morphology plays an important part in coating applicability. All surfaces are flat and homogeneous, without any large protrusions or indents. However, the surfaces are not entirely smooth – they are made from crystallites (Fig. 10). Another notable feature are the pores, which are present in all samples to a higher or lower degree. The 5-layer yttrium compound samples especially look rougher, more uneven, more porous. This does not apply to terbium samples, where the 15-layer coating surface morphology looks more porous, while the 5-layer coating looks less flat. Porosity and pore characteristics of the materials could likely be optimized depending on required use, as it can be controlled by modifying sol concentration and synthesis temperature [89].

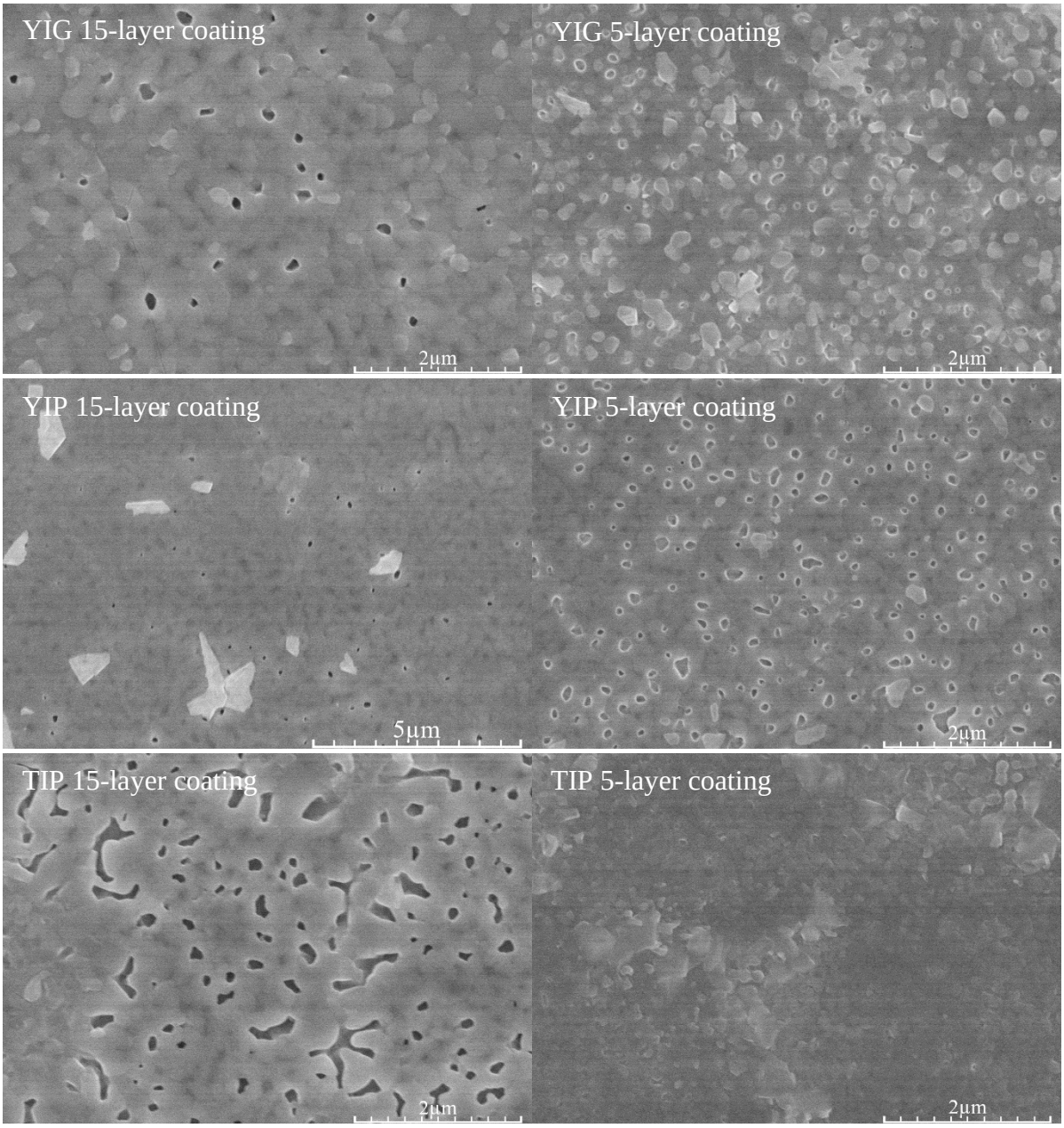

Figure 10. SEM micrographs of indicated coatings (made by dip coating).

SEM was also used to measure coating thickness. This was performed by snapping the sample in half, then using a specialized sample holder that allows to look at the snapped edge. The thickness itself was then measured using ImageJ software. An example of the measurement is displayed in Fig. 11. Thickness was measured multiple times for each sample in different places. The summary of results can be found in Table 1. It should be pointed out that for dip coating, the coating thickness can be different when comparing the side which was at the top during the withdrawal process and the one that was at the bottom, so that contributes to an increased measurement range. Crystallites or other surface irregularities, roughness and similar factors can also contribute to measurement distortions.

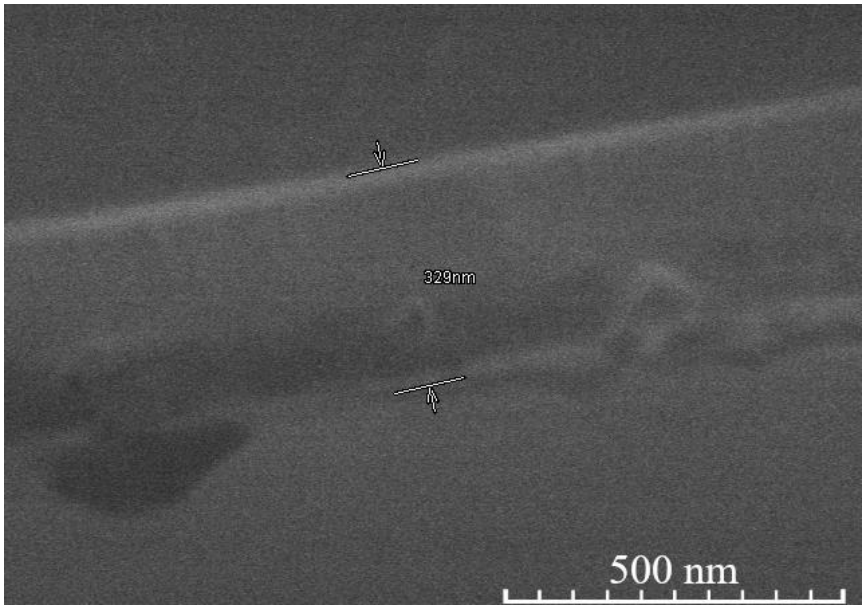

Figure 11. Dip coating 5-layer yttrium iron perovskite (YIP) sample. SEM image of a cross-section of the sample snapped through the middle for layer thickness measurement.

Table 1. YIG, YIP and TIP 15- and 5-layer coating thickness measurement summary (dip coating) and analysis.

		Thickness range, nm	Average thickness, nm	Thickness median, nm	Short analysis*
15-layer	YIG	380-472	424	416	Mostly even surface. No noticeable pores or cavities. Difficult to measure.
	YIP	485-559	511	506	Moderately uneven surface. Few pores, some cavities visible.
	TIP	358-414	386	385	Thinner than yttrium compound coatings. Mostly even surface. Cavities or pores clearly visible.
5-layer	YIG	201-342	273	280	Uneven surface, some unusually large or small crystallites on the surface expand thickness range in addition to dip coating. No hidden cavities visible.
	YIP	261-354	307	316	Even surface. Few cavities or pores visible.
	TIP	216-256	233	234	Thinner than yttrium compound coatings. Even surface, thickness variations due to nature of dip coating. No hidden cavities visible.

*Note that cavities/pores may have formed not necessarily during synthesis, but potentially during the snapping process as well, so should be taken into account in conjunction with regular SEM images.

Thickness measurements show results mostly in line with what could be expected – TIP coatings have an average thickness of 233 nm at 5 layers, and 356 nm average thickness at 15 layers. YIP coatings are about 307 nm thick if 5 layers were used, 511 nm thick if 15 layers. For YIG, the 5-layer coating sample has 273 nm average thickness, while the 15-layer coating has a thickness of 424 nm. These numbers should be taken as approximate, since due to the nature of the measurement, the sample size is relatively limited (16 measurements for each sample), and since the cross-section is not equally visible at all points, the data can be slightly skewed towards the thinner or the thicker side, even if the measurements were done trying to take these this into account and take about a similar amount of measurements from each end and the middle.

Even so, the measurements do provide some insight into coating thickness. Yttrium iron garnet coatings were thinner than yttrium iron perovskite coatings, despite the same number of layers. Terbium sample had a lower concentration solution, so naturally, the layer thickness was also lower. The results indicate that the layer thickness can be controlled well both by modifying the number of layers and the concentrations of the solutions. They also show about the range within which the thickness of the coatings made by this synthesis can be expected to be.

3.3.2. Nanotubes

Nanotube SEM images (Fig. 12) were acquired in order to see if nanotubes formed in the first place. Also to evaluate their quality, thickness and any other defining features.

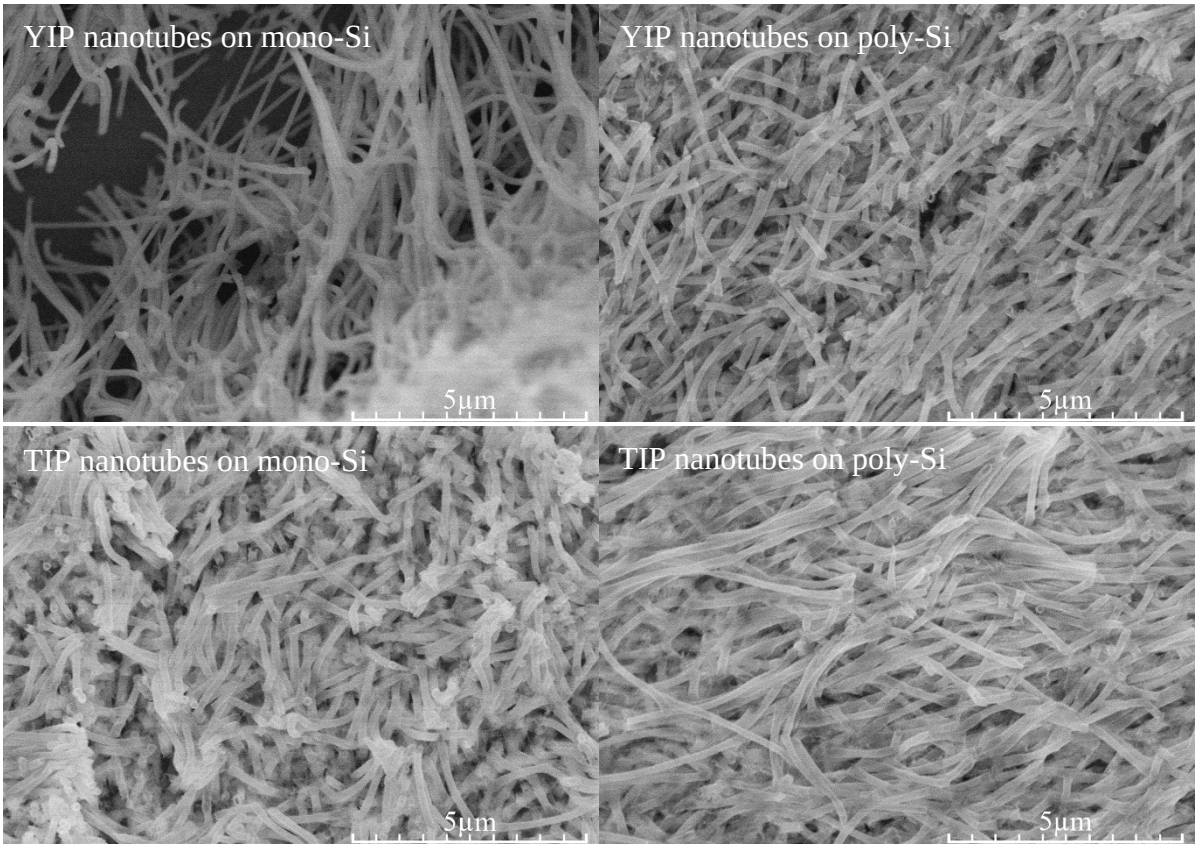

Figure 12. SEM micrographs of indicated nanotubes prepared by heating at 550°C.

Nanotubes heated at 550°C did not have a clear or defined crystal structure, except some very vague hints of some kind of nascent ordering, as was revealed by XRD analysis of these samples (Fig. 7) and discussed earlier. Despite this, they have a very clear and nicely defined nanotube shape, as was revealed by SEM. This is quite surprising, as it means that these nanotubes, despite having a well-defined shape, are mostly amorphous. Even more surprising is the fact that for garnet samples, no nanotube formation was visible at all, even if the only difference between the solution used for perovskite and garnet nanotubes was the stoichiometry, though this could be explained by higher temperature requirements for garnet phase formation. It is also surprising that the nanotubes on polycrystalline silicon and monocrystalline silicon show different results, which indicates that the surface exhibits at least some influence on the length and ordering of the nanotubes, and likely participates in their formation to some degree. Of course, lack of repeatability in the experiment could not be ruled out completely, due to the nature of membrane assisted synthesis. In any case, the formation of these mostly amorphous nanotubes is certainly an interesting discovery.

One last notable feature was that for one sample – YIP on mono-Si – the nanotubes arranged themselves into a macrostructure, as can be seen at lower magnification in Fig. 13.

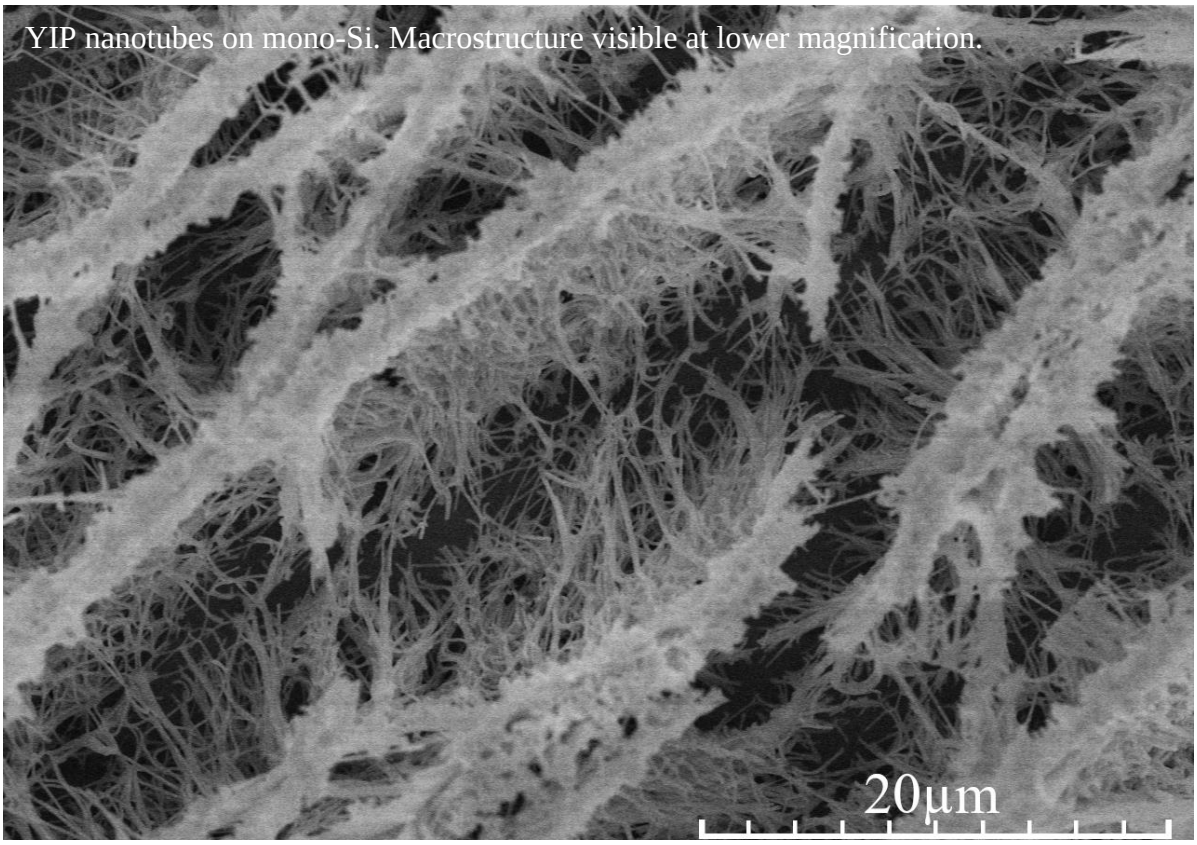

Figure 13. SEM micrograph of the same YIP sample on monocrystalline silicon as in Fig. 12, but at a lower magnification, revealing the macrostructure.

The cause of this remains unclear, since, as will be discussed later, synthesis at a higher temperature, where XRD showed a clearly defined crystal structure, did not show this macrostructure. That is not to say that such macrostructure phenomena are unheard of – magnetic nanomaterials are known to be able to arrange themselves into macrostructures, especially under magnetic fields [90,91]. Rather, it is

unexpected in this case, because the sample did not show a clear crystal structure, and it did not occur in the other samples or in samples synthesised at a higher temperature. It remains unclear whether this is a result of synthesis conditions or magnetic properties.

SEM images of nanotubes heated at 800°C were mostly similar to those heated at 550°C, with several notable differences (Fig. 14).

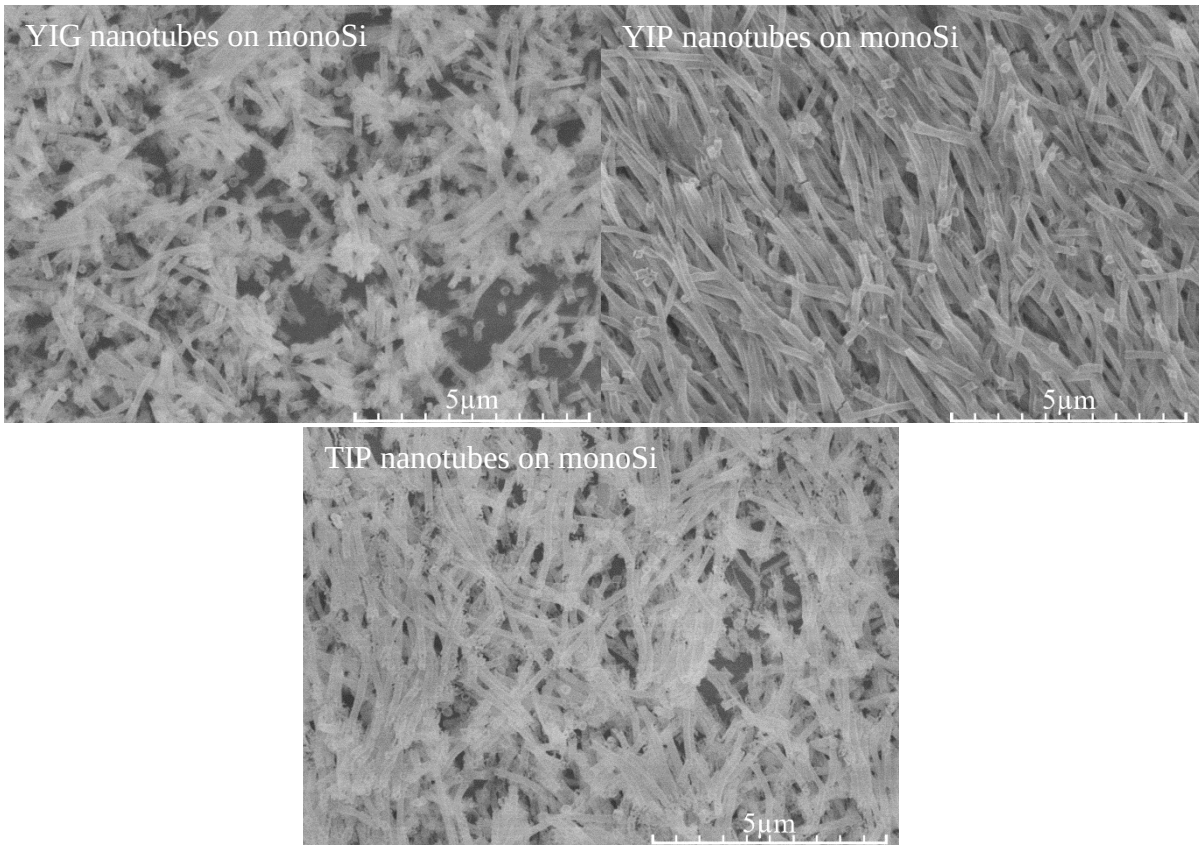

Figure 14. SEM micrographs of indicated nanotubes prepared by heating at 800°C.

One was that YIG nanotubes, which did not form when heating the samples to 550°C, formed when the heating temperature was changed to 800°C, albeit the nanotubes were short and somewhat broken up, and the garnet phase was not clear, as discussed earlier (Fig. 5). TIP nanotubes meanwhile look almost identical to those heated at 550°C, despite completely different XRD results. YIP nanotubes, on the other hand, showed a couple of significant differences in their SEM images – the nanotubes heated at a higher temperature did not display the macrostructure. However, they did show another interesting feature – they were all oriented along a single axis, which can be a significant finding for some uses, since normally, nanotubes form without clear ordering in a single direction. It is unclear what caused this exactly, but the result repeated itself in repeated experiments, meaning it is most likely a feature of this particular synthesis or material rather than some kind of irregularity.

Layering several membranes atop one another in order to increase the quantity of nanotubes formed did not reduce their quality significantly, at least not in a way that could be identified by SEM images or XRD analysis (as mentioned earlier, XRD results showed an improvement due to repeated heating), as can be seen in Fig. 15.

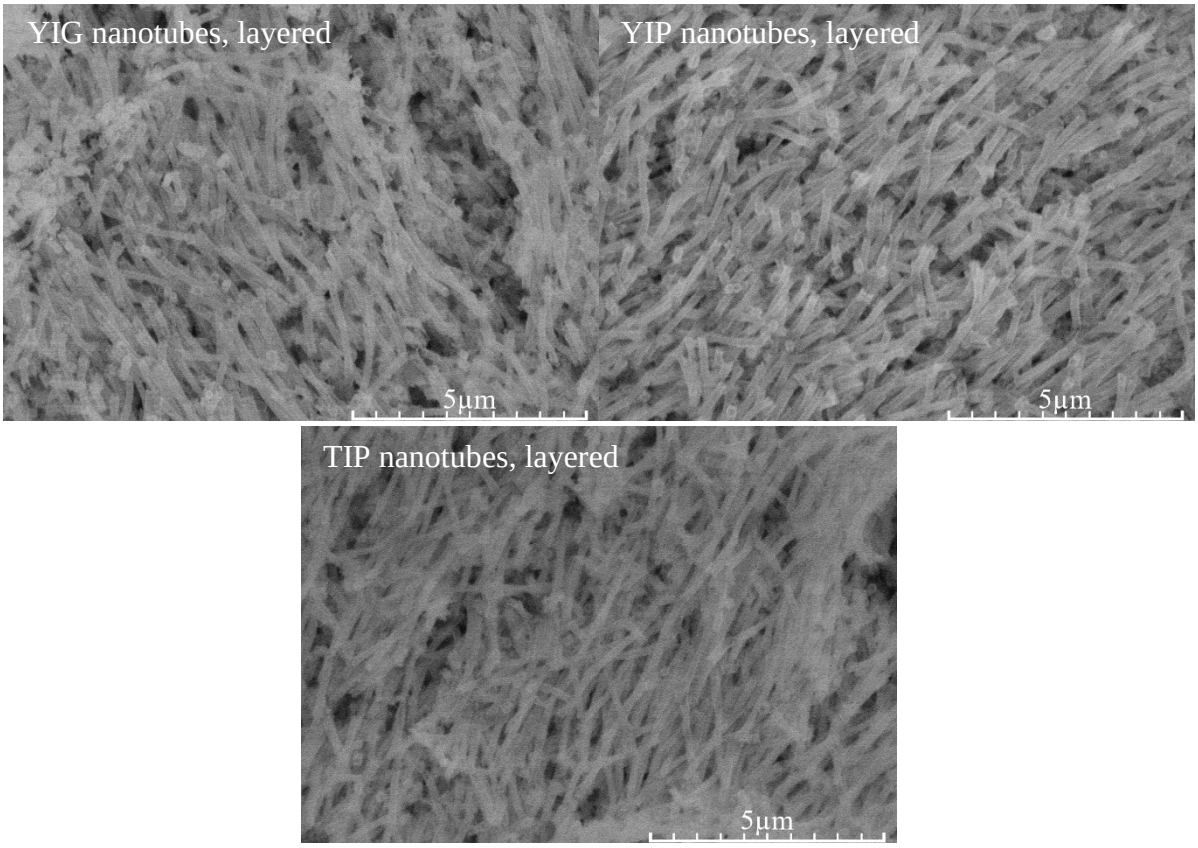

Figure 15. SEM micrographs of YIG, YIP and TIP nanotubes, with three layers of the membrane stacked up one after another (sintering carried out after each layer), heated at 800°C.

However, this does not confirm without a doubt that the nanotube quality did not deteriorate – SEM may not reveal the nanotubes that are at the bottom, hidden underneath the ones at the top, and those may be sintered or otherwise reduced in quality over repeated heating. It does not mean they are, but the possibility cannot be ruled out. One more feature to point out is that YIP nanotubes still displayed the ordering along a single axis, if not quite as expressed as in the case when membranes were not layered.

The size of nanomaterials is a very important parameter that can determine their properties. Often, nanomaterials are considered those that have one of the parameters <100 nm. A broader definition includes all structures smaller than a micrometre, though the definition “sub-micron structures” can then be used. So perhaps it is most productive to consider the context of the specific field, and where the point at which new behaviour can emerge is. In the case of magnetic materials, which are the focus of this work, interesting effects can be observed when particle size approaches domain size (between 1 nm and 1000 nm) or domain wall width (between 1 nm and several hundred nm), thus it is probably fair to call materials that fall somewhere within this range nanomaterials in this context [92,93]. Nanotube size was determined with the aid of SEM imaging (example in Fig. 16).

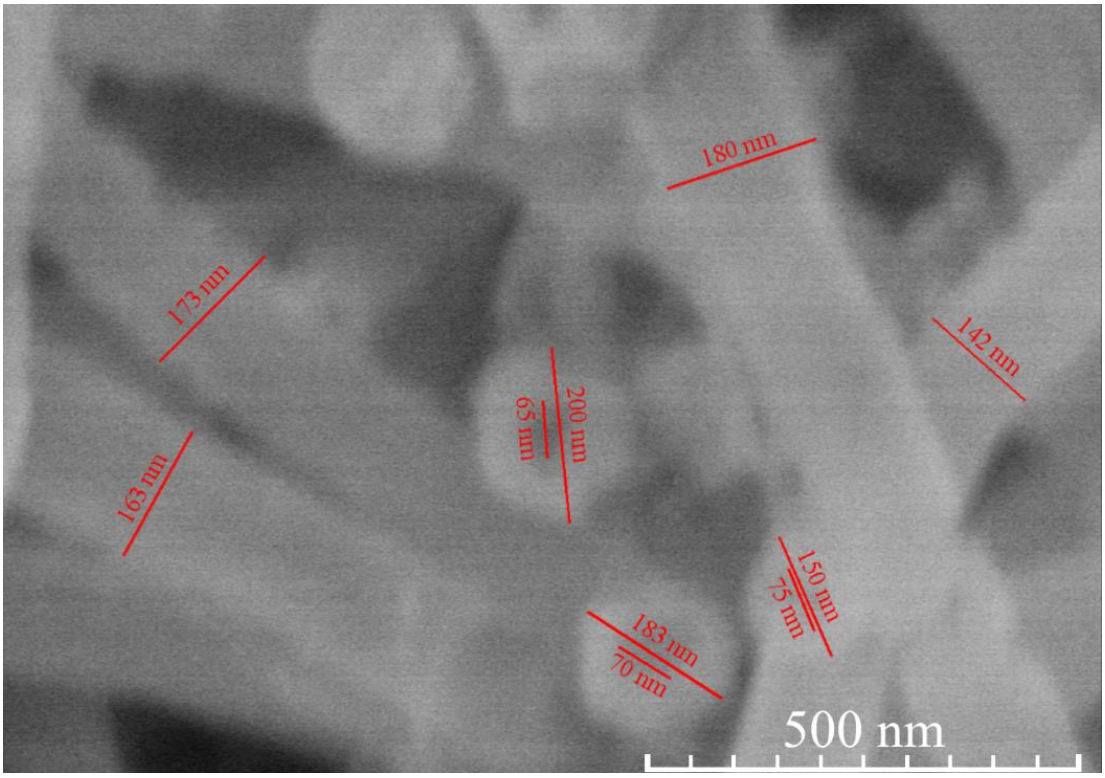

Figure 16. Example of nanotube thickness measurements. Sample with larger nanotubes was chosen for more clarity.

The main drawback of this, of course, is a relatively small sample size. Even so, at least tentative results can be obtained that provide some insight into the size range. The diameter measured varied in the range of about 100-200 nm, depending on the sample (more detailed information in Table 2). Most nanotubes had a greater diameter at the ends, were thinner around the middle. Nanotube wall thickness was difficult to measure, since it required a conveniently positioned nanotube facing upwards, so there were too few samples to create any kind of meaningful averaging or draw solid conclusions. Because of this, only a single measurement of nanotube wall thickness is provided for each sample. It ranges in the area of about 25-50 nm. No definite nanotube length could be determined, since the nanotubes tend to overlap, with one end hidden among other nanotubes, and only the other end visible. However, a complete nanotube was visible in one YIP 800° sample – its length was about 3.5 μm (impossible to determine how representative this is of the majority, however). Also, in one YIG 800°C sample, which had a noticeably higher number of broken nanotube pieces and had shorter nanotubes, quite a sizeable number of complete nanotubes were visible, and were in the range of 1-1.2 μm, though some were longer, having visible ends over this range, with unidentified length remaining hidden. For other samples, clues that would help determine at least the minimum nanotube size were summarised (in Table 2) – mostly by considering the length of the visible part of the nanotube, and pointing out that the rest may not have been visible.

Table 2. YIG, YIP and TIP nanotube size and parameter measurement summary; brief quality and length analysis included.

		Nanotube diameter range, nm	Average nanotube diameter, nm	Example tube wall thickness, nm	Nanotube length, quality analysis, short description. (note that usually, nanotubes were intertwined, so entire length was not visible)
550°C	MonoSi Substrate YIP	113-151	124	15	At least 4.5 µm length nanotubes visible, but could be longer as they get hidden underneath each other by that point.
	PolySi substrate YIP	125-165	138	21	A large amount or shorter nanotubes in the range of 1.5-1.8 µm visible.
	MonoSi Substrate TIP	133-175	146	27.5	Majority at least 3 µm or longer, hidden underneath each other, so how long exactly could not be determined.
	PolySi substrate TIP	119-200	142	26.5	Majority at least 3 µm or longer, hidden underneath each other, so how long exactly could not be determined.
800°C	YIG	126-177	140	43	Many shorter, 1.5 µm tubes visible, some longer with hidden ends. A moderate amount of broken nanotube pieces present.
	YIP	129-161	145	50	Majority at least 2 µm visible, some 3.5, ends hidden underneath each other, so how long exactly could not be determined.
	TIP	118-192	142	50	Many shorter, 1.5 µm tubes visible, some longer with hidden ends. Some broken nanotube pieces present.
800°C, layered	YIG	134-168	141	43	Many shorter, 1-1.2 µm tubes visible. More broken nanotube pieces and artifacts than in other samples.
	YIP	136-165	155	50	Majority at least 3.5 µm visible, ends hidden underneath each other, so how long exactly could not be determined.
	TIP	118-171	136	24	Majority at least 3.5 µm visible, ends hidden underneath each other, so how long exactly could not be determined.

3.4. Atomic force microscopy

Atomic force microscopy measurements were also carried out for the initial batch of 5-layer and 15-layer dip coating samples, as a complementary measurement for SEM and also to determine surface roughness. The structure seen by AFM imaging (Fig. 17) is reminiscent of that seen by SEM, even if the surface morphology is not quite as visible. What can be determined better, however, is how prevalent and how expressed the pores and protrusions are.

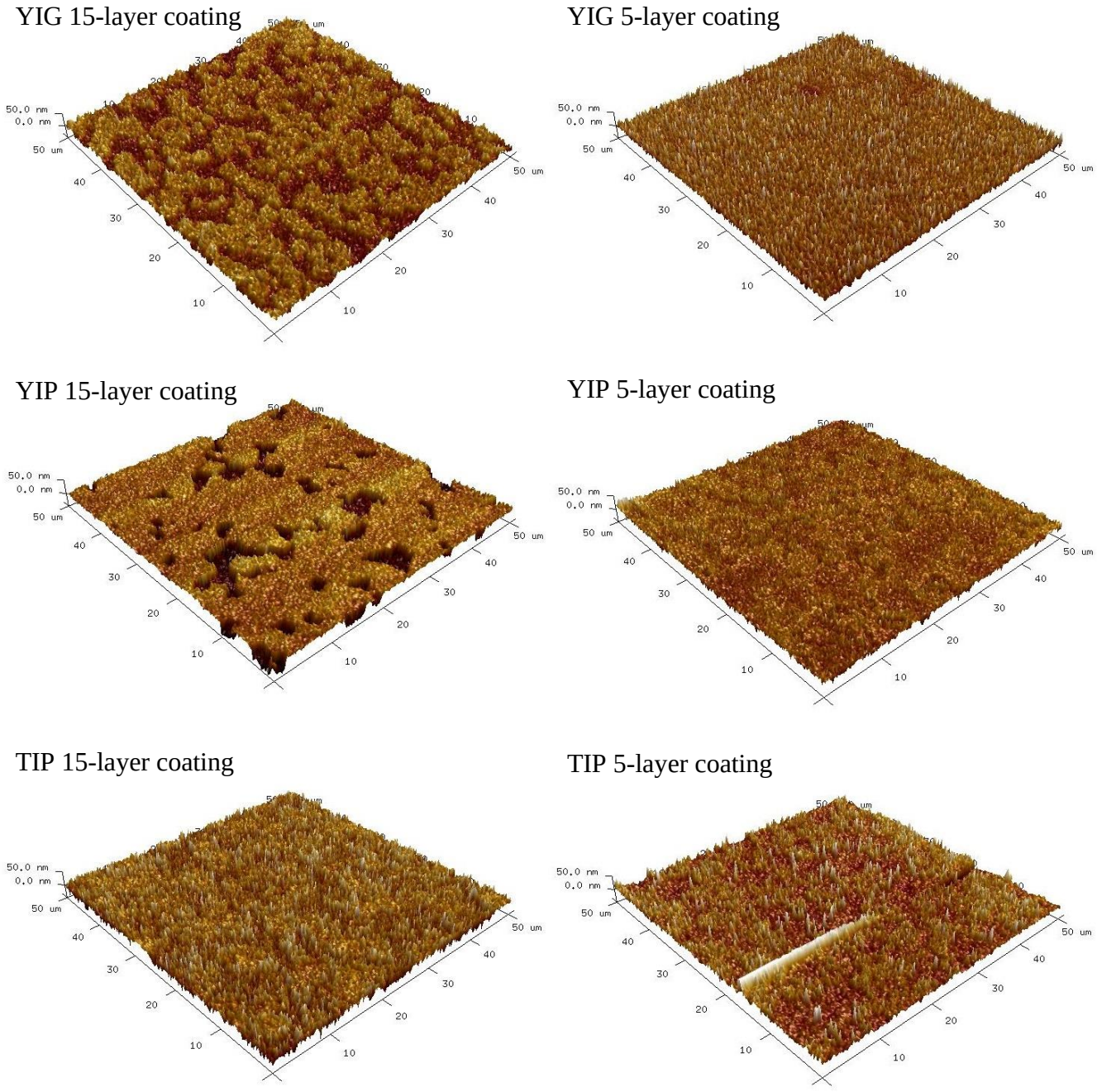

Figure 17. 3D AFM images of indicated dip coating samples.

Table 3. AFM surface roughness measurements for dip-coated samples.

	R_q, nm	R_a, nm
YIG 15-layer sample	10.7	8.7
YIG 5-layer sample	10.1	7.9
YIP 15-layer sample	12.5	8.8
YIP 5-layer sample	8.56	6.5
TIP 15-layer sample	13.6	10.7
TIP 5-layer sample	10.6	7.1

R_q here stands for root mean square roughness, R_a for overall average roughness. Roughness itself is the measurement of how much, in nanometres, the peaks and cavities deviate from a flat surface – how rough the surface is. Whether high or low roughness is preferable depends on each particular application, but it is always useful to know what a chosen synthesis method can produce. In this case, we see an average surface roughness (R_a) that stays in the range of 6-11 nm for most samples. This is a surprisingly low deviation range, considering how different the images looked, especially in SEM imaging, and it could be easy to assume that roughness had a high variance as well. These results show that that is not the case; roughness only experiences a minor increase with increasing layer number (which is to be expected – more layers mean more potential deviation), and seems to have no conclusive dependence on the material used. The greatest determinant of this parameter, therefore, is most likely the chosen synthesis procedure and its parameters. This means that if the need to modify surface roughness in either direction would arise (depending on potential application), further experimentation could be done in this area.

3.5. Mossbauer spectroscopy and magnetic measurements

Mossbauer spectroscopy could be performed, since iron was one of the constituents of the compounds. From a structural evaluation perspective, that is especially helpful in this case, since in XRD analysis some peaks overlap, and any additional clues whether assumptions made from the previously acquired results are correct are welcome. Also, it can sometimes provide additional insights into some other properties, such as the magnetic structure.

Mossbauer spectroscopy results for pure powders show well-defined multiplets characteristic of the materials. YIG has Fe in two different positions within the crystal structure, which results in two characteristic overlapping patterns as can be seen in Fig. 18 b). Perovskite structure, meanwhile, has only one Fe position, so patterns for both perovskites look similar, but again, they are what could be expected. This is in agreement with data obtained from XRD, showing that what seem to be pure phases are obtained, and also provide a basis for easier comparison to other Mossbauer spectra.

Fig. 19 shows the Mossbauer spectrum of samples where dip coating was performed on monocrystalline silicon. Since coatings have very little material, the signal for Mossbauer spectroscopy is rather weak. Even so, it still provides useful data. What is immediately apparent (especially when comparing to Fig. 18), is that garnet phase is present in all samples. However, the spectrum is different than that for pure garnet phase. While alone that would not be enough to draw solid conclusions, when considering the spectrum in conjunction with XRD data (Fig. 5), it seems to reinforce the assumption that garnet is the dominant phase, with small amounts of perovskite present, for all dip coating samples.

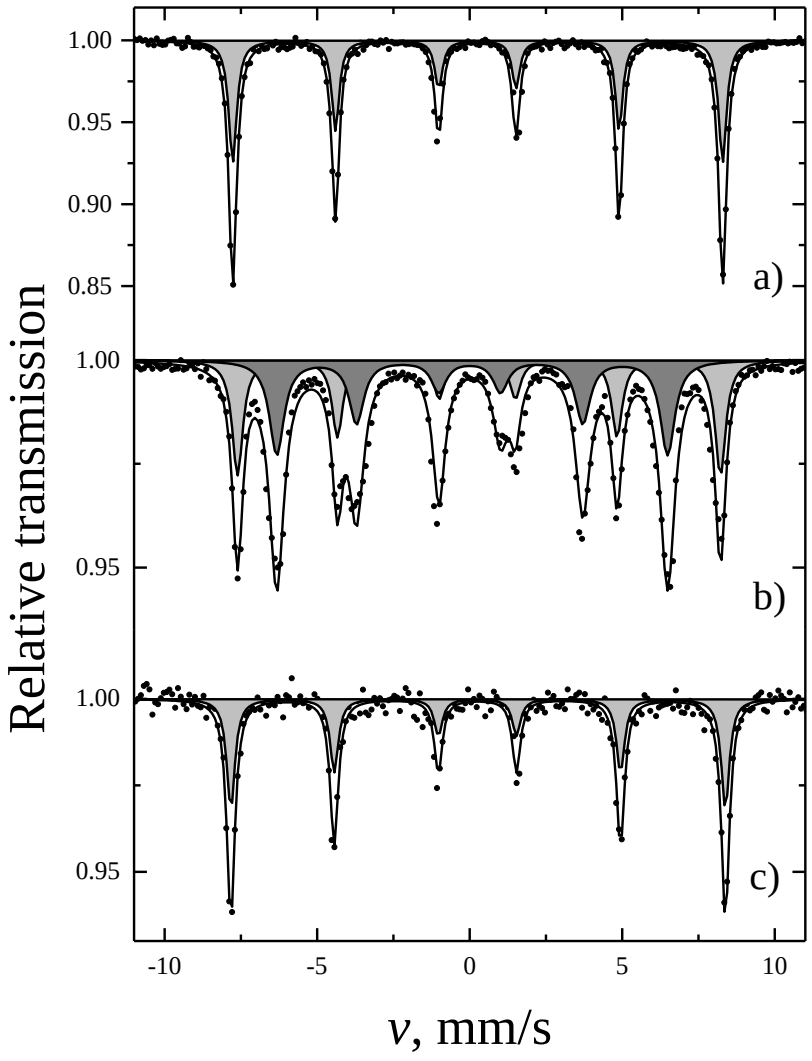

Figure 18. Mossbauer spectroscopy data of a) YIP powder, b) YIG powder and c) TIP powder at room temperature.

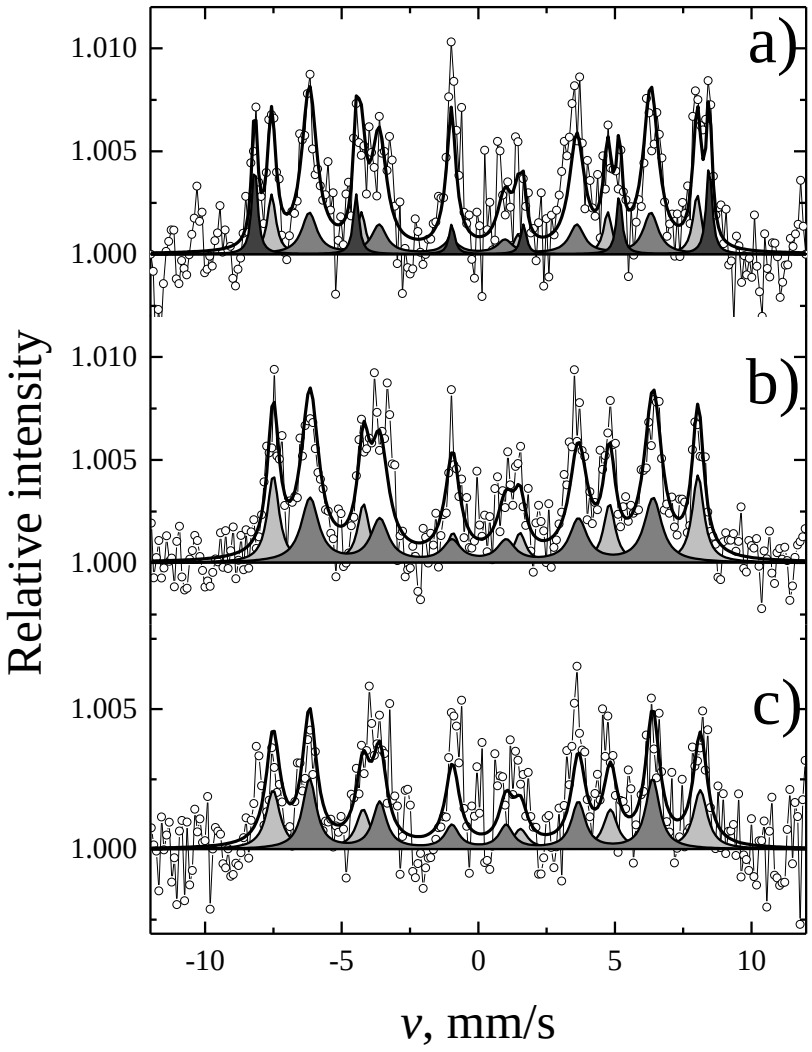

Figure 19. Mossbauer spectra of 15-layer coatings made by the dip coating procedure. a) YIG, b) YIP, c) TIP.

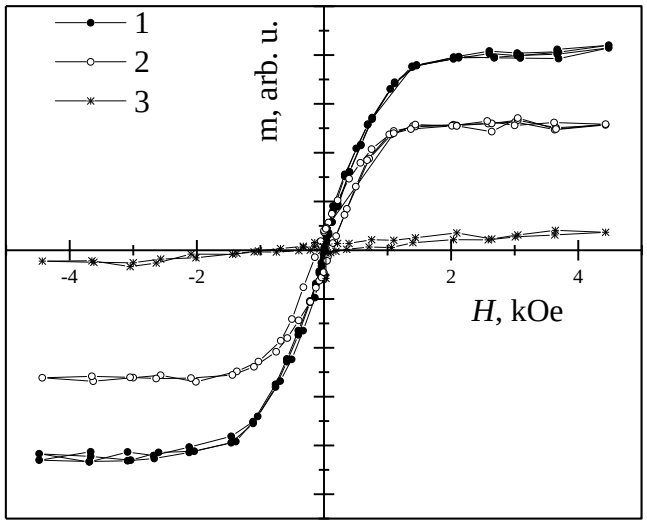

Figure 20. Magnetization hysteresis of 15-layer coatings made by dip coating 1) YIG, 2) YIP, 3) TIP.

Magnetic hysteresis measurements (Fig. 20) of the first three 15-layer coatings (dip coating) show saturation magnetisation that is characteristic for the ferrimagnetic YIG phase, which is unsurprising, considering that XRD and Mossbauer data indicated it being the dominant phase. The ferrimagnetism from garnet likely overshadows any influence from the most-likely antiferromagnetic [23] (or potentially weakly ferrimagnetic) perovskite phase. Saturation magnetisation for terbium sample is most likely also due to terbium iron garnet, since both Mossbauer and XRD data indicate that garnet phase formed for the terbium compound as well. It is several orders of magnitude lower than for the other phases. Also, while it is difficult to compare definitely without knowing the exact amount of material that makes up each coating, but considering that their substrates were the same size, and that average thickness is actually higher for YIP coating (Table 1) than for YIG coating, the possibility exists that the lower magnetisation seen for YIP compound seen in Fig. 20 could be a consequence of a slightly lower ratio of YIG formed as compared to YIP. This would indicate that perhaps changing dip coating conditions might also allow to obtain coatings of desired stoichiometry. And while the data is nowhere near solid enough to confirm this, the possibility could be considered if more data supporting this difference were to appear.

CONCLUSIONS

1. Simple aqueous sol-gel processing using nitrate precursors was a suitable synthesis route for the preparation of high purity powders of yttrium iron garnet, yttrium iron perovskite and terbium iron perovskite, as determined by XRD analysis and Mossbauer spectroscopy.
2. The application of the same sol-gel route using a dip coating technique was problematic for the fabrication of thin films of the same compounds. Monophasic compounds were not obtained. The results of XRD analysis and Mossbauer spectroscopy indicated that garnet was the dominant phase in the thin films obtained, showing that phase composition of the coatings did not correlate to the stoichiometry of metals in the sol.
3. It was demonstrated that using a spin coating process, a different phase composition was obtained.
4. SEM micrographs of dip coating samples revealed a polycrystalline coating structure, with varying degrees of porosity visible in all coatings.
5. Coating thickness of dip coated samples was determined by SEM. 5-layer coating thickness was approximately 200-300 nm. 15-layer coating thickness was approximately 400-500 nm. Average surface roughness, as determined by AFM was in the range of 6-11 nm.
6. Magnetic hysteresis measurements of dip coated samples showed clear ferrimagnetism for both yttrium samples characteristic of yttrium iron garnet. For terbium sample, saturation magnetisation was several orders of magnitude lower, but likely caused by terbium iron garnet.
7. Successful membrane assisted synthesis of nanotubes from the same adapted sol-gel method was also developed. Nanotubes from both perovskite sols formed during the synthesis at 550°C and were visible by SEM. Nanotube synthesis at 800°C was successful with all the sols for all desired compounds. XRD in this case showed clear, monophasic compounds. SEM imaging confirmed the nanotube structure.
8. The diameter of nanotubes synthesised at 800°C was in the range of 100-200 nm for all samples, with some small variance. Nanotube length was difficult to determine exactly due to their intertwined nature, but fragments at least 3.5 μm in length were visible for most perovskite samples, while garnet produced shorter nanotubes which were then easier to measure and were about 1-1.5 μm in length depending on sample. Wall thickness could not be measured with any accuracy, but most measurements fell into the range of 20-50 nm.
9. Slight upscaling of the nanotube synthesis by layering three membranes, an additional one after each heating step, showed no quality deterioration that could be identified by SEM imaging or XRD analysis.

SUMMARY

VILNIUS UNIVERSITY
FACULTY OF CHEMISTRY AND GEOSCIENCES
DEPARTMENT OF APPLIED CHEMISTRY

JUSTINAS JANUŠKEVIČIUS

Synthesis and characterization of yttrium and terbium iron perovskites and yttrium iron garnet

Master thesis

Garnet and perovskite structures are among the most promising in the field of ceramics for many new or developing technologies. Yttrium iron garnet, in particular, is already well known and used for its characteristic magnetic properties. Perovskites, meanwhile, have been leading improvements in a variety of fields – photovoltaics, catalysis, sensors, superconductivity and – more recently – have shown promise in the resurgent field of multiferroics. Creating new technologies like that is especially important, because some that are used today are nearing theoretical limits in regards to what can be improved. Because of this, large efforts are being made in order to find new compounds with useful properties that could enable this innovation, and also to find simple but potent synthesis routes that would allow to create desired structures from these materials, as that can heavily impact both their properties and applicability.

Current work attempts to delve into this area. The three compounds investigated – garnet $Y_3Fe_5O_{12}$ and perovskites $YFeO_3$ and $TbFeO_3$ are either already used or show promise for their magnetic properties. In this work, it is shown that a simple aqueous sol-gel route using inorganic salt precursors is capable of producing pure powders of these materials, and that it can also be adapted -with varying degrees of success- to create coatings by using dip coating or spin coating procedures, which are standard in an industrial setting. It also shows that the same sol-gel process is versatile enough that it can also be adapted, through a membrane-assisted method, to produce nanotubes that have a well-defined structure. The gel used for the production of powders is investigated by thermogravimetric method to evaluate the temperatures of the main processes occurring during heating. X-ray diffraction is used to identify phase purity of the powders, coatings and nanotubes, with some help from Mossbauer spectroscopy in some cases. Scanning electron microscopy is used to examine surfaces and thickness of dip coating samples, also nanotube size and other features. Atomic force microscopy is also employed to determine the roughness of the dip coating samples. Magnetic measurements were carried out for some of the coatings.

SANTRAUKA

VILNIAUS UNIVERSITETAS
CHEMIJOS IR GEOMOKSLŲ FAKULTETAS
TAIKOMOSIOS CHEMIJOS KATEDRA

JUSTINAS JANUŠKEVIČIUS

Itrio ir terbio geležies perovskitų bei itrio geležies granato sintezė ir apibūdinimas

Magistrinis darbas

Granatų bei perovskitų struktūros junginiai yra tarp perspektyviausių medžiagų kuriant įvairias naujas bei tobulinant esamas technologijas. Itrio geležies granatas yra plačiai naudojamas dėl jam būdingų magnetinių savybių. Įvairūs perovskitai naudojami kurti naujoves saulės elementų, katalizės, sensorių ir superlaidininkų srityse. Paskutiniu metu jų panaudojimas tapo labai perspektyvus atgijusioje multiferoikos srityje. Norint sukurti įvairias naujas technologijas, dažnai ypač svarbu yra pirmiau sukurti šiuolaikines medžiagas, pasižyminčias įvairiomis naudingomis savybėmis, kurios leistų vystytis šioms inovacijoms. Taip pat labai svarbu yra kurti naujus, paprastus, efektyvius, ekonomiškus, pigius sintezės metodus, kuriais būtų galima susintetinti norimas šių medžiagų struktūras, kadangi nuo to gali stipriai priklausyti jų savybės bei taikomumas.

Šiame pristatome darbe yra susintetintos ir ištirtos trys medžiagos – itrio geležies granatas, itrio geležies perovskitas bei terbio geležies perovskitas. Jau dabar jos naudojamos, arba potencialiai gali būti pritaikomos dėl savo magnetinių savybių. Šiame darbe parodyta, kad šie vienfaziai junginiai miltelių pavidale gali būti susintetinti paprastu zolių-gelių metodu. Taip pat atskleista, jog šis metodas, naudojant pamerkimo bei sukimo dengimo technologijas, kurios dažnai naudojamos ir pramonėje, gali būti pritaikytas gaminti šių junginių plonoms dangoms, kurios randa specifinį taikymą aukštųjų technologijų srityje. Taip pat parodyta, kad tas pats zolių-gelių procesas, naudojant membranos šablono metodą, yra pakankamai universalus, kad galėtų būti pritaikytas ir gerai apibrėžtos struktūros nanovamzdelių gamybai. Darbe pristatomi gelių, naudotų keramikinių miltelių sintezei, termogravimetrinės analizės rezultatai, parodantys pagrindinius vyksmus kaitinimo metu. Rentgeno spindulių difrakcinė analizė, ir kai kuriais atvejais Mossbauer spektroskopija, panaudotos nustatyti susintetintų miltelių, dangų bei nanovamzdelių fazinį grynumą. Skenuojanti elektroninė mikroskopija panaudota ištirti pamerkimo metodu pagamintų dangų paviršių morfologiją bei sluoksnių storį, taip pat nanovamzdelių dydį bei kitus parametrus. Atominės jėgos mikroskopija panaudota dangų paviršiaus šiurkštumui nustatyti. Taip pat tirtos kai kurių dangų magnetinės savybės.

REFERENCES

[1] J. Wang, J. Zhang, Y. Zhou, H. Liu, Q. Xue, X. Li, C.C. Chueh, H.L. Yip, Z. Zhu, A.K.Y. Jen, Highly efficient all-inorganic perovskite solar cells with suppressed non-radiative recombination by a Lewis base, Nature Communications. 11, 177 (2020). https://doi.org/10.1038/s41467-019-13909-5.

[2] M.A. Green, A. Ho-Baillie, H.J. Snaith, The emergence of perovskite solar cells, Nature Photonics. 8 (2014) 506–514. https://doi.org/10.1038/nphoton.2014.134.

[3] A. Maity, A.K. Raychaudhuri, B. Ghosh, High sensitivity NH3 gas sensor with electrical readout made on paper with perovskite halide as sensor material, Scientific Reports. 9 (2019) 7777. https://doi.org/10.1038/s41598-019-43961-6.

[4] J.W. Fergus, Perovskite oxides for semiconductor-based gas sensors, Sensors and Actuators, B: Chemical. 123 (2007) 1169–1179. https://doi.org/10.1016/j.snb.2006.10.051.

[5] R.J. Cava, B. Batlogg, R.B. van Dover, D.W. Murphy, S. Sunshine, T. Siegrist, J.P. Remeika, E.A. Rietman, S. Zahurak, G.P. Espinosa, Bulk superconductivity at 91 K in single-phase oxygen-deficient perovskite Ba2YCu3O9−δ, Physical Review Letters. 58 (1987) 1676–1679. https://doi.org/10.1103/PhysRevLett.58.1676.

[6] M.H.K. Rubel, A. Miura, T. Takei, N. Kumada, M. Mozahar Ali, M. Nagao, S. Watauchi, I. Tanaka, K. Oka, M. Azuma, E. Magome, C. Moriyoshi, Y. Kuroiwa, A.K.M. Azharul Islam, Superconducting double perovskite bismuth oxide prepared by a low-temperature hydrothermal reaction, Angewandte Chemie - International Edition. 53 (2014) 3599–3603. https://doi.org/10.1002/anie.201400607.

[7] L.F. Schneemeyer, J.V. Waszczak, S.M. Zahorak, R.B. van Dover, T. Siegrist, Superconductivity in rare earth cuprate perovskites, Materials Research Bulletin. 22 (1987) 1467–1473. https://doi.org/10.1016/0025-5408(87)90211-X.

[8] B.R. Sutherland, E.H. Sargent, Perovskite photonic sources, Nature Photonics. 10 (2016) 295–302. https://doi.org/10.1038/nphoton.2016.62.

[9] P. Kanhere, Z. Chen, A review on visible light active perovskite-based photocatalysts, Molecules. 19 (2014) 19995–20022. https://doi.org/10.3390/molecules191219995.

[10] C. Li, X. Lu, W. Ding, L. Feng, Y. Gao, Z. Guo, Formability of ABX 3 (X = F, Cl, Br, I) halide perovskites, Acta Crystallographica B. 64(Pt. 6) (2008) 702–707. https://doi.org/10.1107/S0108768108032734.

[11] S.A. Veldhuis, P.P. Boix, N. Yantara, M. Li, T.C. Sum, N. Mathews, S.G. Mhaisalkar, Perovskite Materials for Light-Emitting Diodes and Lasers, Advanced Materials. 28 (2016) 6804–6834. https://doi.org/10.1002/adma.201600669.

[12] G. Li, Z.K. Tan, D. Di, M.L. Lai, L. Jiang, J.H.W. Lim, R.H. Friend, N.C. Greenham, Efficient Light-Emitting Diodes Based on Nanocrystalline Perovskite in a Dielectric Polymer Matrix, Nano Letters. 15 (2015) 2640–2644. https://doi.org/10.1021/acs.nanolett.5b00235.

[13] G. Wang, D. Li, H.C. Cheng, Y. Li, C.Y. Chen, A. Yin, Z. Zhao, Z. Lin, H. Wu, Q. He, M. Ding, Y. Liu, Y. Huang, X. Duan, Wafer-scale growth of large arrays of perovskite microplate crystals for functional electronics and optoelectronics, Science Advances. 1 (2015). https://doi.org/10.1126/sciadv.1500613.

[14] Q. Chen, J. Wu, X. Ou, B. Huang, J. Almutlaq, A.A. Zhumekenov, X. Guan, S. Han, L. Liang, Z. Yi, J. Li, X. Xie, Y. Wang, Y. Li, D. Fan, D.B.L. Teh, A.H. All, O.F. Mohammed, O.M. Bakr, T. Wu, M. Bettinelli, H. Yang, W. Huang, X. Liu, All-inorganic perovskite nanocrystal scintillators, Nature. 561 (2018) 88–109. https://doi.org/10.1038/s41586-018-0451-1.

[15] Y. Lee, J. Kwon, E. Hwang, C.H. Ra, W.J. Yoo, J.H. Ahn, J.H. Park, J.H. Cho, High-performance perovskite-graphene hybrid photodetector, Advanced Materials. 27 (2015) 41–46. https://doi.org/10.1002/adma.201402271.

[16] R.R. Subkhangulov, R. v. Mikhaylovskiy, A.K. Zvezdin, V. v. Kruglyak, T. Rasing, A. v. Kimel, Terahertz modulation of the Faraday rotation by laser pulses via the optical Kerr effect, Nature Photonics. 10 (2016) 111–114. https://doi.org/10.1038/nphoton.2015.249.

[17] A.D. Lozano-Gorrín, U.R. Rodríguez-Mendoza, V. Venkatramu, V. Monteseguro, M.A. Hernández-Rodríguez, I.R. Martín, V. Lavín, Lanthanide-doped Y3Ga5O12 garnets for nanoheating and nanothermometry in the first biological window, Optical Materials. 84 (2018) 46–51. https://doi.org/10.1016/j.optmat.2018.06.043.

[18] N.G. Park, Perovskite solar cells: An emerging photovoltaic technology, Materials Today. 18 (2015) 65–72. https://doi.org/10.1016/j.mattod.2014.07.007.

[19] H.W. Lee, K.C. Kim, J. Lee, Review of Maglev train technologies, IEEE Transactions on Magnetics. 42 (2006) 1917–1925. https://doi.org/10.1109/TMAG.2006.875842.

[20] S. Hong, O. Auciello, D. Wouters, eds., Emerging non-volatile memories, Springer US, 2014. https://doi.org/10.1007/978-1-4899-7537-9.

[21] N.A. Hill, Why are there so few magnetic ferroelectrics?, Journal of Physical Chemistry B. (2000). https://doi.org/10.1021/jp000114x.

[22] S.A. Wolf, D.D. Awschalom, R.A. Buhrman, J.M. Daughton, S. von Molnár, M.L. Roukes, A.Y. Chtchelkanova, D.M. Treger, Spintronics: A spin-based electronics vision for the future, Science. 294 (2001) 1488–1495. https://doi.org/10.1126/science.1065389.

[23] O. Rosales-González, F. Sánchez-De Jesús, C.A. Cortés-Escobedo, A.M. Bolarín-Miró, Crystal structure and multiferroic behavior of perovskite YFeO3, Ceramics International. 44 (2018) 15298–15303. https://doi.org/10.1016/j.ceramint.2018.05.175.

[24] M. Shang, C. Zhang, T. Zhang, L. Yuan, L. Ge, H. Yuan, S. Feng, The multiferroic perovskite YFeO3, Applied Physics Letters. 102 (2013) 062903. https://doi.org/10.1063/1.4791697.

[25] P. Szuromi, B. Grocholski, Natural and engineered perovskites, Science. 358 (2017) 732–733. https://doi.org/10.1126/science.358.6364.732.

[26] E.A.R. Assirey, Perovskite synthesis, properties and their related biochemical and industrial application, Saudi Pharmaceutical Journal. 27 (2019) 817–829. https://doi.org/10.1016/j.jsps.2019.05.003.

[27] H. Liu, X. Yang, A brief review on perovskite multiferroics, Ferroelectrics. 507 (2017) 69–85. https://doi.org/10.1080/00150193.2017.1283171.

[28] C.J. Bartel, C. Sutton, B.R. Goldsmith, R. Ouyang, C.B. Musgrave, L.M. Ghiringhelli, M. Scheffler, New tolerance factor to predict the stability of perovskite oxides and halides, Science Advances. 5 (2019). https://doi.org/10.1126/sciadv.aav0693.

[29] J. Akhtar, M. Aamir, M. Sher, Organometal lead halide perovskite, in: T. Sabu, T. Aparna (Eds.), Perovskite Photovoltaics: Basic to Advanced Concepts and Implementation, Academic Press, 2018: pp. 25–42. https://doi.org/10.1016/B978-0-12-812915-9.00002-2.

[30] S. Mitra, ABX3, Perovskite-ilmenite structure, in: Developments in Geochemistry, Elsevier, 2004: pp. 711–792. https://doi.org/10.1016/S0921-3198(04)80012-7.

[31] X. Zheng, L. Zhang, Photonic nanostructures for solar energy conversion, Energy and Environmental Science. 9 (2016) 2511–2532. https://doi.org/10.1039/c6ee01182a.

[32] C. Li, K.C.K. Soh, P. Wu, Formability of ABO3 perovskites, Journal of Alloys and Compounds. 372 (2004) 40–48. https://doi.org/10.1016/j.jallcom.2003.10.017.

[33] T. Sato, S. Takagi, S. Deledda, B.C. Hauback, S.I. Orimo, Extending the applicability of the Goldschmidt tolerance factor to arbitrary ionic compounds, Scientific Reports. 6 (2016) 23592. https://doi.org/10.1038/srep23592.

[34] K.Y. Tsui, N. Onishi, R.F. Berger, Tolerance Factors Revisited: Geometrically Designing the Ideal Environment for Perovskite Dopants, Journal of Physical Chemistry C. 120 (2016) 23293–23298. https://doi.org/10.1021/acs.jpcc.6b09277.

[35] K.S. Aleksandrov, J. Bartolomé, Structural distortions in families of perovskite-like crystals, Phase Transitions. 74 (2001) 255–335. https://doi.org/10.1080/01411590108228754.

[36] D. Beqiri, V. Cascos, J. Roberts-Watts, E.R. Clark, E. Bousquet, N.C. Bristowe, E.E. McCabe, Tuning octahedral tilts and the polar nature of: A-site deficient perovskites, Chemical Communications. 55 (2019) 2609–2612. https://doi.org/10.1039/c8cc10126d.

[37] N. Nuraje, K. Su, Perovskite ferroelectric nanomaterials, Nanoscale. 5 (2013) 8752–8780. https://doi.org/10.1039/c3nr02543h.

[38] H. Röhm, T. Leonhard, A.D. Schulz, S. Wagner, M.J. Hoffmann, A. Colsmann, Ferroelectric Properties of Perovskite Thin Films and Their Implications for Solar Energy Conversion, Advanced Materials. 31 (2019) 1806661. https://doi.org/10.1002/adma.201806661.

[39] H. Tanaka, N. Okawa, T. Kawai, Magnetic exchange interactions in perovskite LaMnO3/LaMO3 (M = Ni, Co, Cr, Fe) superlattices, Solid State Communications. 110 (1999) 191–196. https://doi.org/10.1016/S0038-1098(99)00068-X.

[40] D. Yang, P. Zhao, S. Huang, T. Yang, D. Huo, Ferrimagnetism, resistivity, and magnetic exchange interactions in double perovskite La2CrMnO6, Results in Physics. 12 (2019) 344–348. https://doi.org/10.1016/j.rinp.2018.11.090.

[41] T. Zheng, J. Wu, D. Xiao, J. Zhu, Recent development in lead-free perovskite piezoelectric bulk materials, Progress in Materials Science. 98 (2018) 552–624. https://doi.org/10.1016/j.pmatsci.2018.06.002.

[42] Q. Ou, X. Bao, Y. Zhang, H. Shao, G. Xing, X. Li, L. Shao, Q. Bao, Band structure engineering in metal halide perovskite nanostructures for optoelectronic applications, Nano Materials Science. 1 (2019) 268–287. https://doi.org/10.1016/j.nanoms.2019.10.004.

[43] J.G. Bednorz, K.A. Müller, Perovskite-Type Oxides—the New Approach to High-Tc Superconductivity. Nobel Lecture., Angewandte Chemie International Edition in English. 27 (1988) 735–748. https://doi.org/10.1002/anie.198807351.

[44] M. Oudah, A. Ikeda, J.N. Hausmann, S. Yonezawa, T. Fukumoto, S. Kobayashi, M. Sato, Y. Maeno, Superconductivity in the antiperovskite Dirac-metal oxide Sr3-x SnO, Nature Communications. 7 (2016) 13617. https://doi.org/10.1038/ncomms13617.

[45] M.A. Gilleo, Ferromagnetic insulators: Garnets, in: Handbook of Ferromagnetic Materials, Vol. 2, Elsevier, 1980: pp. 1–53. https://doi.org/10.1016/S1574-9304(05)80102-6.

[46] C.P. Khattak, F.F.Y. Wang, Perovskites and garnets, in: Handbook on the Physics and Chemistry of Rare Earths, Vol. 3, Elsevier, 1979: pp. 525–607. https://doi.org/10.1016/S0168-1273(79)03012-9.

[47] T. Fujii, Y. Sakabe, Growth and Magnetic Properties of YIG Films, in: K.H.J. Buschow, R.W. Cahn, M.C. Flemings, B. Ilschner, E.J. Kramer, S. Mahajan, P. Veyssière (Eds.), Encyclopedia of Materials: Science and Technology, 2nd ed., Elsevier, 2001: pp. 3666–3670. https://doi.org/10.1016/b0-08-043152-6/00654-9.

[48] Z. Frukacz, D.A. Pawlak, Garnets, Growth of, in: K.H.J. Buschow, R.W. Cahn, M.C. Flemings, B. Ilschner, E.J. Kramer, S. Mahajan, P. Veyssière (Eds.), Encyclopedia of Materials: Science and Technology, 2nd ed., Elsevier, 2001: pp. 3455–3463. https://doi.org/10.1016/b0-08-043152-6/00616-1.

[49] J.F. Ready, Practical Lasers, in: Industrial Applications of Lasers, 2nd ed., Academic Press, 1997: pp. 66–130. https://doi.org/10.1016/b978-012583961-7/50005-3.

[50] T. Boudiar, B. Payet-Gervy, M.F. Blanc-Mignon, J.J. Rousseau, M. le Berre, H. Joisten, Magneto-optical properties of yttrium iron garnet (YIG) thin films elaborated by radio frequency sputtering, Journal of Magnetism and Magnetic Materials. 284 (2004) 77–85. https://doi.org/10.1016/j.jmmm.2004.06.046.

[51] M.C. Onbasli, L. Beran, M. Zahradník, M. Kucera, R. Antoš, J. Mistrík, G.F. Dionne, M. Veis, C.A. Ross, Optical and magneto-optical behavior of Cerium Yttrium Iron Garnet thin films at wavelengths of 200-1770 nm, Scientific Reports. 6 (2016) 23640. https://doi.org/10.1038/srep23640.

[52] A.M. Grishin, S.I. Khartsev, All-Garnet Magneto-Optical Photonic Crystals, Journal of the Magnetics Society of Japan. 32 (2008) 140–145. https://doi.org/10.3379/msjmag.32.140.

[53] R. Riedel, I.W. Chen, eds., Ceramics Science and Technology, Wiley-VCH, 2013. https://doi.org/10.1002/9783527631940.

[54] S. Sakka, Sol-Gel Process and Applications, in: S. Somiya (Ed.), Handbook of Advanced Ceramics: Materials, Applications, Processing, and Properties, 2nd ed., Academic Press, 2013: pp. 883–910. https://doi.org/10.1016/B978-0-12-385469-8.00048-4.

[55] P.P. Phulé, T.E. Wood, Ceramics and Glasses, Sol–Gel Synthesis of, in: K.H.J. Buschow, R.W. Cahn, M.C. Flemings, B. Ilschner, E.J. Kramer, S. Mahajan, P. Veyssière (Eds.), Encyclopedia of Materials: Science and Technology, Elsevier, 2001: pp. 1090–1095. https://doi.org/10.1016/b0-08-043152-6/00201-1.

[56] A.E. Danks, S.R. Hall, Z. Schnepp, The evolution of “sol-gel” chemistry as a technique for materials synthesis, Materials Horizons. 3 (2016) 91–112. https://doi.org/10.1039/c5mh00260e.

[57] S. Esposito, “Traditional” sol-gel chemistry as a powerful tool for the preparation of supported metal and metal oxide catalysts, Materials. 12 (2019) 668. https://doi.org/10.3390/ma12040668.

[58] M. Niederberger, Aqueous and Nonaqueous Sol-Gel Chemistry, in: Metal Oxide Nanoparticles in Organic Solvents. Engineering Materials and Processes., Springer London, 2009: pp. 7–18. https://doi.org/10.1007/978-1-84882-671-7_2.

[59] T. Woignier, J. Phalippou, F. Despetis, S. Calas-Etienne, Aerogel processing, in: L. Klein, M. Aparicio, A. Jitianu (Eds.), Handbook of Sol-Gel Science and Technology: Processing, Characterization and Applications, Springer International Publishing, 2018: pp. 985–1011. https://doi.org/10.1007/978-3-319-32101-1_27.

[60] G.W. Scherer, Xerogels, in: J. Buschow, R.W. Cahn, M.C. Flemings, B. Ilschner, E.J. Kramer, S. Mahajan, P. Veyssière (Eds.), Encyclopedia of Materials: Science and Technology, 2nd ed., Elsevier, 2001: pp. 9797–9799. https://doi.org/10.1016/b0-08-043152-6/01777-0.

[61] C.J. Brinker, G.C. Frye, A.J. Hurd, C.S. Ashley, Fundamentals of sol-gel dip coating, Thin Solid Films. 201 (1991) 97–108. https://doi.org/10.1016/0040-6090(91)90158-T.

[62] J.E. ten Elshof, Chemical solution deposition techniques for epitaxial growth of complex oxides, in: G. Koster, M. Huijben, G. Rijnders (Eds.), Epitaxial Growth of Complex Metal Oxides, Woodhead Publishing, 2015: pp. 69–93. https://doi.org/10.1016/B978-1-78242-245-7.00004-X.

[63] D.P. Birnie, Spin Coating Technique, in: Sol-Gel Technologies for Glass Producers and Users, Springer US, 2004: pp. 49–55. https://doi.org/10.1007/978-0-387-88953-5_4.

[64] J. Puetz, M.A. Aegerter, Dip Coating Technique, in: M.A. Aegerter, M. Mennig (Eds.), Sol-Gel Technologies for Glass Producers and Users, Springer US, Boston, MA, 2004: pp. 37–48. https://doi.org/10.1007/978-0-387-88953-5_3.

[65] M.A. Aegerter, M. Mennig, eds., Sol-Gel Technologies for Glass Producers and Users, Springer US, 2004. https://doi.org/10.1007/978-0-387-88953-5.

[66] C. Kittel, Introduction to Solid State Physics, 8th ed., John Wiley & Sons, Ltd (10.1111), 1953.

[67] S.H. Simon, Solid State Basics, Oxford University Press, 2013.

[68] K.J. Edler, Formation of Ordered Mesoporous Thin Films Through Templating, in: L. Klein, M. Aparicio, A. Jitianu (Eds.), Handbook of Sol-Gel Science and Technology, Springer International Publishing, 2017: pp. 1–67. https://doi.org/10.1007/978-3-319-19454-7_26-1.

[69] S. Blundell, Magnetism in condensed matter, Oxford University Press, 2001.

[70] D.A.B. Miller, Quantum Mechanics for Scientists and Engineers, Cambridge University Press, 2012. https://doi.org/10.1017/CBO9780511813962.

[71] A.P. French, E.F. Taylor, An Introduction to Quantum Physics, 1st ed., W. W. Norton & Company, 1979. https://doi.org/10.1119/1.11656.

[72] P. Anikeeva, G. Beach, N. Holten-Anderson, 3.024 Electronic, Optical and Magnetic Properties of Materials. Spring 2013. Massachusetts Institute of Technology: MIT OpenCourseWare, https://ocw.mit.edu., (n.d.).

[73] F. Duan, J. Guojun, Introduction to condensed matter physics, Volume 1, World Scientific Publishing Co., 2005. https://doi.org/10.1142/5435.

[74] J. Lu, A. Günther, F. Schrettle, F. Mayr, S. Krohns, P. Lunkenheimer, A. Pimenov, V.D. Travkin, A.A. Mukhin, A. Loidl, On the room temperature multiferroic BiFeO 3: Magnetic, dielectric and thermal properties, European Physical Journal B. (2010). https://doi.org/10.1140/epjb/e2010-00170-x.

[75] P. Barone, S. Picozzi, Multiferroics: theory, mechanisms, and materials, Science and Technology of Atomic, Molecular, Condensed Matter & Biological Systems. 2 (2012) 129–161. https://doi.org/10.1016/B978-0-44-453681-5.00006-6.

[76] M. Shang, L. Yuan, H. Yuan, C. Zhang, T. Zhang, S. Feng, L. Ge, The multiferroic perovskite YFeO 3, Applied Physics Letters. 102 (2013) 062903. https://doi.org/10.1063/1.4791697.

[77] M. Fiebig, T. Lottermoser, D. Meier, M. Trassin, The evolution of multiferroics, Nature Reviews Materials. 1 (2016) 16046. https://doi.org/10.1038/natrevmats.2016.46.

[78] O. Opuchovic, S. Culunlu, A.U. Morkan, I.A. Morkan, D. Niznansky, E. Garskaite, A. Beganskiene, A. Kareiva, Structural, morphological, and magnetic characterization of bulk and thin films Y3Al5–xFexO12 (YAIG): From the perspective of aqueous sol–gel processing, Chemical Engineering Communications. 204 (2017) 1037–1048. https://doi.org/10.1080/00986445.2017.1336091.

[79] O. Opuchovic, A. Beganskiene, A. Kareiva, Sol-gel derived Tb3Fe5O12 and Y3Fe5O12 garnets: Synthesis, phase purity, micro-structure and improved design of morphology, Journal of Alloys and Compounds. 647 (2015) 189–197. https://doi.org/10.1016/j.jallcom.2015.05.169.

[80] O. Opuchovic, G. Kreiza, J. Senvaitiene, K. Kazlauskas, A. Beganskiene, A. Kareiva, Sol-gel synthesis, characterization and application of selected sub-microsized lanthanide (Ce, Pr, Nd, Tb) ferrites, Dyes and Pigments. 118 (2015) 176–182. https://doi.org/10.1016/j.dyepig.2015.03.017.

[81] L. Alinauskas, E. Brooke, A. Regoutz, A. Katelnikovas, R. Raudonis, S. Yitzchaik, D.J. Payne, E. Garskaite, Nanostructuring of SnO2 via solution-based and hard template assisted method, Thin Solid Films. 626 (2017) 38–45. https://doi.org/10.1016/j.tsf.2017.02.015.

[82] A. Hooda, M.S. Goyat, J.K. Pandey, A. Kumar, R. Gupta, A review on fundamentals, constraints and fabrication techniques of superhydrophobic coatings, Progress in Organic Coatings. 142 (2020). https://doi.org/10.1016/j.porgcoat.2020.105557.

[83] S. Roy, S.B. Majumder, Recent advances in multiferroic thin films and composites, Journal of Alloys and Compounds. 538 (2012) 153–159. https://doi.org/10.1016/j.jallcom.2012.05.125.

[84] D. Grosso, How to exploit the full potential of the dip-coating process to better control film formation, Journal of Materials Chemistry. 21 (2011) 17033. https://doi.org/10.1039/c1jm12837j.

[85] Y. Guo, M. Li, W. Zhao, D. Akai, K. Sawada, M. Ishida, M. Gu, Ferroelectric and pyroelectric properties of (Na0.5Bi0.5)TiO3–BaTiO3 based trilayered thin films, Thin Solid Films. 517 (2009) 2974–2978. https://doi.org/10.1016/j.tsf.2008.11.100.

[86] J. He, ed., Self-cleaning Coatings, Royal Society of Chemistry, Cambridge, 2016. https://doi.org/10.1039/9781782623991.

[87] C.K. Jeong, J.H. Lee, D.Y. Hyeon, Y. gyu Kim, S. Kim, C. Baek, G.J. Lee, M.K. Lee, J.J. Park, K. il Park, Piezoelectric energy conversion by lead-free perovskite BaTiO3 nanotube arrays fabricated using electrochemical anodization, Applied Surface Science. 512 (2020) 144784. https://doi.org/10.1016/j.apsusc.2019.144784.

[88] X.J. Wu, F. Zhu, C. Mu, Y. Liang, L. Xu, Q. Chen, R. Chen, D. Xu, Electrochemical synthesis and applications of oriented and hierarchically quasi-1D semiconducting nanostructures, Coordination Chemistry Reviews. 254 (2010) 1135–1150. https://doi.org/10.1016/j.ccr.2010.02.014.

[89] K. Zheng, A.R. Boccaccini, Sol-gel processing of bioactive glass nanoparticles: A review, Advances in Colloid and Interface Science. (2017). https://doi.org/10.1016/j.cis.2017.03.008.

[90] S. Rosenfeldt, S. Förster, T. Friedrich, I. Rehberg, B. Weber, Self-Assembly of Magnetic Iron Oxide Nanoparticles Into Cuboidal Superstructures, in: Novel Magnetic Nanostructures, Elsevier, 2018: pp. 165–189. https://doi.org/10.1016/B978-0-12-813594-5.00005-9.

[91] C. Jiang, C.W. Leung, P.W.T. Pong, Magnetic-Field-Assisted Assembly of Anisotropic Superstructures by Iron Oxide Nanoparticles and Their Enhanced Magnetism, Nanoscale Research Letters. 11 (2016) 189. https://doi.org/10.1186/s11671-016-1406-9.

[92] F. Nasirpouri, A. Nogaret, Nanomagnetism and spintronics: Fabrication, materials, characterization and applications, 2010. https://doi.org/10.1142/7281.

[93] R. Skomski, Length Scales in Magnetism, in: Encyclopedia of Materials: Science and Technology, Elsevier, 2006: pp. 1–7. https://doi.org/10.1016/b0-08-043152-6/02115-x.

ACKNOWLEDGEMENT

I would like to thank dr. Dalis Baltrūnas and dr. Kęstutis Mažeika from the Centre for Physical Sciences and Technology, who carried out Mossbauer spectroscopy and magnetic hysteresis measurements and were a great help.